Master of Science Thesis

Development of a semi-empirical thermal conduction estimation model for dry metal-metal contacts

Akshra Sharma

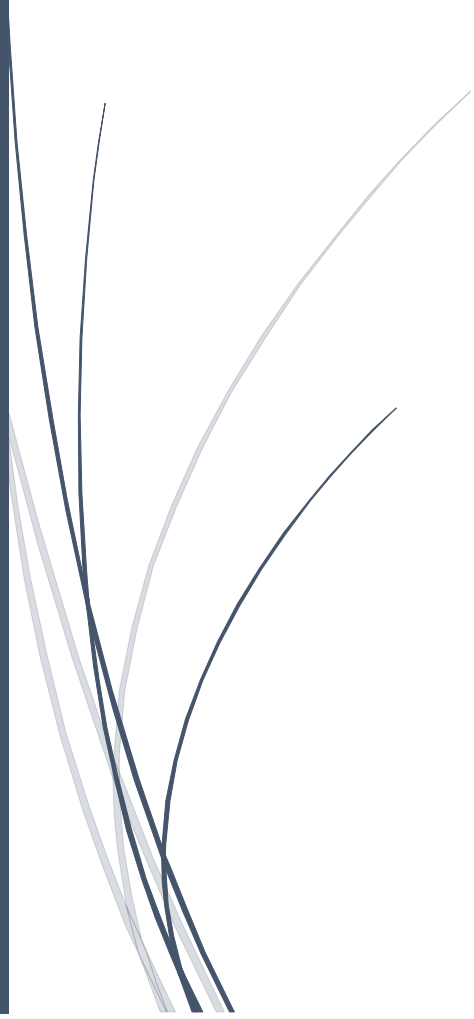

Development of a semi-empirical thermal conduction estimation model for dry metal-metal contacts

Master of Science Thesis

For the degree of Master of Science in Energy, Flow and Process Technology at Delft University of Technology

Akshra Sharma

5205581

April 18, 2023

Supervisors:

Dr René Delfos [T.U. Delft]

Dr. ir. Rob Van Gils [ASML]

Faculty of Mechanical, Maritime and Materials Engineering (3mE).

Delft University of Technology

Acknowledgement

Throughout my journey in this thesis project, I have received immense support and encouragement, and I would like to take this opportunity to thank the following people.

I would like to begin by expressing my profound gratitude towards Dr. Rene Delfos, whose constant support and guidance has made this research possible. I would also like to give my appreciation to Dr. ir. Rob Van Gils for always being ready to help tackle and discuss any and all questions that I had, along with constant supervision.

I would like to thank my parents, they are the source of my strength and determination. Even though we are apart by thousands of miles, they have always shown their love and affection, boosting my morale in uncertain times and giving me the will to carry on.

Finally I would like to thank my friends, who have always been there for me for helping me out and encouraging me in every dull moment.

Akshra Sharma

Delft, April 2023

Abstract

This thesis aims to investigate the effects of contact pressure and type of deformations on the thermal contact conductance(*h'*) for dry metal-metal contacts. Also, an attempt is made to develope a thermal contact conductance estimation model for the same. The materials used in this thesis are metals(aluminium and tin).

Several experiments are performed on two different test setups. The first setup is situated in the process and energy department[P&E] of TU Delft where tin material is used to investigate deformation effects on *h'* with respect to contact pressure ranging till 4MPa. The sample is in a shape of a wire with a diameter 2mm and placed between two copper cylinders for evaluating *h'*. The second setup is situated in Philips Engineering Solutions[PES] where flat aluminium samples are used with different roughness under high contact pressures(up to 25MPa). Later, the results from both experimental setups are compared to the prediction from literature models to brief their general applicability.

The increase in contact pressure over a surface roughness, first deforms a surface elastically and then plastically. Plastic deformation increases the actual contact area and conducts more heat than elastic with sample contact pressure.

Oxide layer formation over time is critical for aluminium surfaces and so aging may cause differences in contact conduction.

In conclusion, there is a large difference between the experimental results and prediction by literature models. Only when a lot of effort is put in keeping orientation exactly the same, reproducibility is good, rest the thermal contact conduction is irreproducible. The development of an entirely new semi-empirical model is very complex. There is a need to be aware of validity ranges of thermal contact conductance literature models as they quickly deteriorate outside their application ranges and the usage of available models should be done critically. The real contact area plays a major role in estimating *h'*.

Contents

Nomenclature

h'	Thermal contact conductance, heat transfer coefficient	$[W/m^2K]$
p	Applied contact pressure	[Pa]
k	Thermal conductivity	[W/mK]
α	Thermal expansion coefficient	[1/K]
E	Modulus of elasticity	[Pa]
E'	Effective modulus of elasticity	[Pa]
T_m	Harmonic Mean temperature	[K]
R_a	Arithmetic average of roughness	[m]
σ	Equivalent root mean square Roughness	[m]
Rz	Averages only the five highest peaks of roughness	[m]
m	Absolute average asperity slope	[-]
m'	Root mean square of asperity slope	[-]
γ	Dimensionless parameter	[-]
H_c	Surface microhardness	$[N/mm^2]$
k_m	harmonic mean thermal conductivity of the interface	[W/mK]
H_v	Vickers hardness	$[N/mm^2]$
H_b	Brinell hardness	$[N/mm^2]$
NTC	Negative Temperature Coefficient Thermistor	[K]
TCC	Thermal Contact Conductance	[-]

Table Of Figures

1 Introduction

1.1.ASML (Advanced Semiconductor Materials Lithography)

The company was founded in the 1980s to cope with the pace of the newly developing semiconductor industry. Now, in 2023 as the leader in producing chip machines, the growth is enormous, yet challenging. Upgrading the machines at a rapid rate requires continuous effort. The machine complexity increases with every upgrade. The machine works on the principle of lithography [Appendix D].

The machines developed are huge and needs enormous supply of energy. Prime materials for the machine base frame are aluminium and steel, which are good conductors of heat and electricity. The overall heat transfer analyses considers the heat losses and irregularities. The basic need is the heat transfer analyses of the whole machine for which we analyse precise heat transfer. This analysis reduces the complexity while upgrading the machine.

Precise heat transfer calculation will help to predict energy consumption more accurately. Thus, this thesis project will indirectly help ASML to achieve its sustainability goals. Regarding environmental impact, there are sustainable goals that ASML aims to achieve by 2025.[1]

- "ASML is committed to minimizing waste and maximizing the use of resources and works closely with our customers and suppliers to achieve this. ASML has set an ambitious target to cut our amount of waste per revenue by 50% by 2025 (compared to 2019)." [1]
- "ASML is committed to taking every step required to lower our carbon footprint. The company's ambition to achieve zero emissions across our operations by 2025." [1]

Figure 1 ASML Electric Ultraviolet (EUV) machine [1]

1.2 Modes of heat transfer

Heat Transfer is the transfer of heat between two physical objects. Generally, the heat is transferred from the object at a higher temperature to the object at a lower temperature. It can happen in 3 different modes [2], as mentioned below:

Conduction – The heat transfer by physical contact is known as conductive heat transfer and happens at the molecular and subatomic scale.

Convection – The transport of energy/heat by the circulation or movement of the heated parts of a liquid or gas.

Radiation – The heat transferred by the photons that travel from one surface to another is known as radiative heat transfer and a well-known example of this is the heat we receive from the Sun.

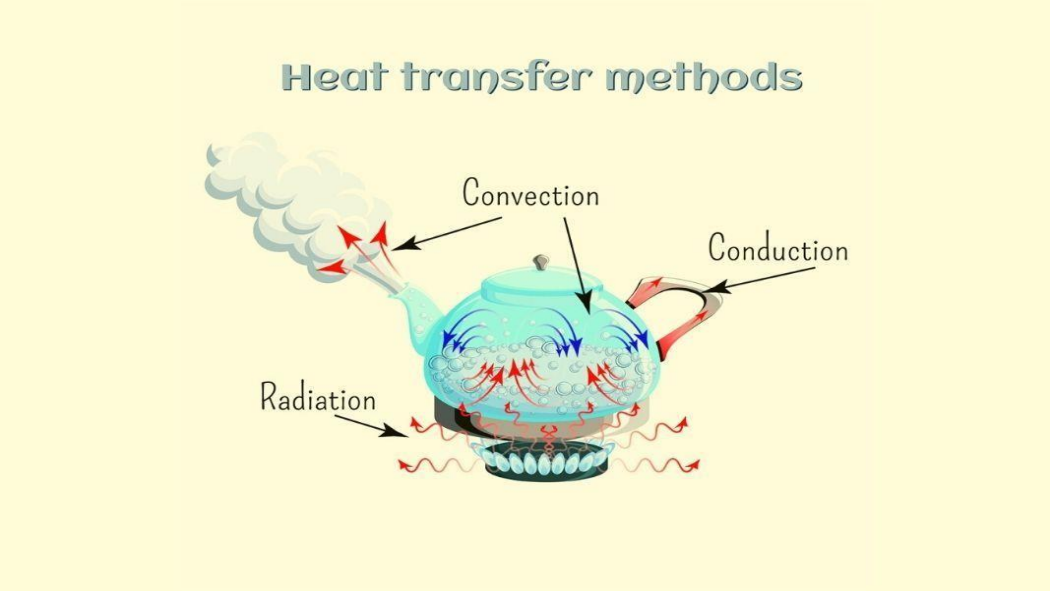

Figure 2 Modes of Heat Transfer

Usually, heat transfer is a combination of all three modes, but analysing and understanding each is entirely different. The focused mode in this report is conduction. Heat transfer through conduction becomes quite complex as it depends upon molecular collisions in gases, lattice vibrations in crystals or the flow of free electrons in metals [2]. Yet it is the simplest mode of heat transfer among the three.

1.2.1 Thermal Contact Conductance

For defining problem introduction, understanding thermal contact conduction is essential.

According to Fourier's law, "The conduction heat flux in a specified direction equals the negative of the product of the medium thermal conductivity and the temperature derivative."

For 1-D dimensional heat flow, we can represent the heat flux as,

$$q = \frac{Q}{A} \; ; \; q = -\frac{kdT}{dx} \tag{1.1}$$

Q = heat flux in x direction [W]

q = heat flux per unit area [W/m^2]

T = local temperature [K or °C]

x = coordinate in heat flow direction [m]

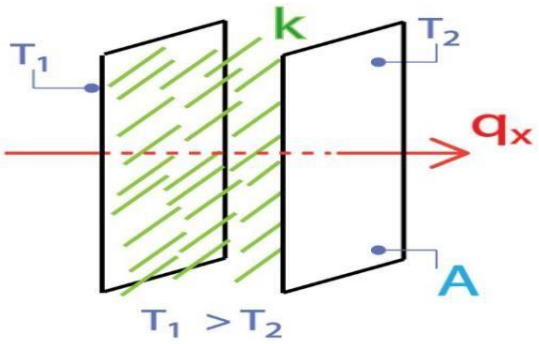

Figure 3 Thermal conduction through a block

When two solid objects are in contact, conduction takes place and thermal resistance to heat flow is called contact resistance(R).

The thermal contact conductance phenomenon considers conductance through the contact area, and its coefficient is h' [W/m^2K]. Contact conductivity is dominant in metals with lower resistance, like aluminium and copper.

$$h' = Q/A(\Delta T) \tag{1.2}$$

$$R = 1/h' \tag{1.3}$$

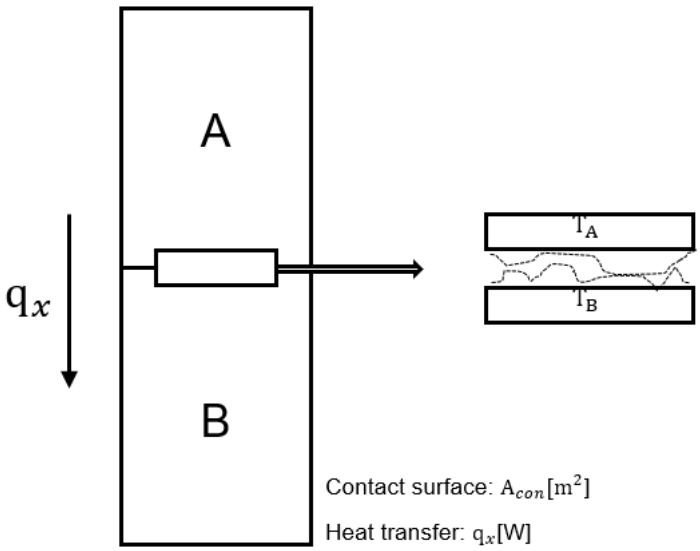

Figure 4 Thermal Contact Conductance

Figure 4 explains the contact conductance phenomenon. The two blocks A and B are in contact. The temperature of block A is T_A and the temperature of block B is T_B. The heat flows from the block with a higher temperature(A) to the block with a lower temperature(B). The contact under a microscope can be seen as two surfaces with different asperity slopes. Asperity slopes are a surface property and surface parameters play a major role in TCC calculations. The opposite of TCC is thermal contact resistance (TCR) and can be expressed as R.

1.3 Problem introduction

This chapter defines the importance of the contact conductance heat transfer phenomenon in the industry. ASML has developed newer generation EUV lithography machines capable of producing more complex chips in the same area. This EUV machine uses a powerful ultraviolet light source that imprints the silicon wafer. The light source imprints the chips by heat, and the energy in heat transfer is to be estimated to make sure the chips work accordingly. There are a lot of areas in EUV machines where TCC phenomenon is dominant, to properly model we need to know their values. For example, the cooling block bolted on the frame of EUV machine.

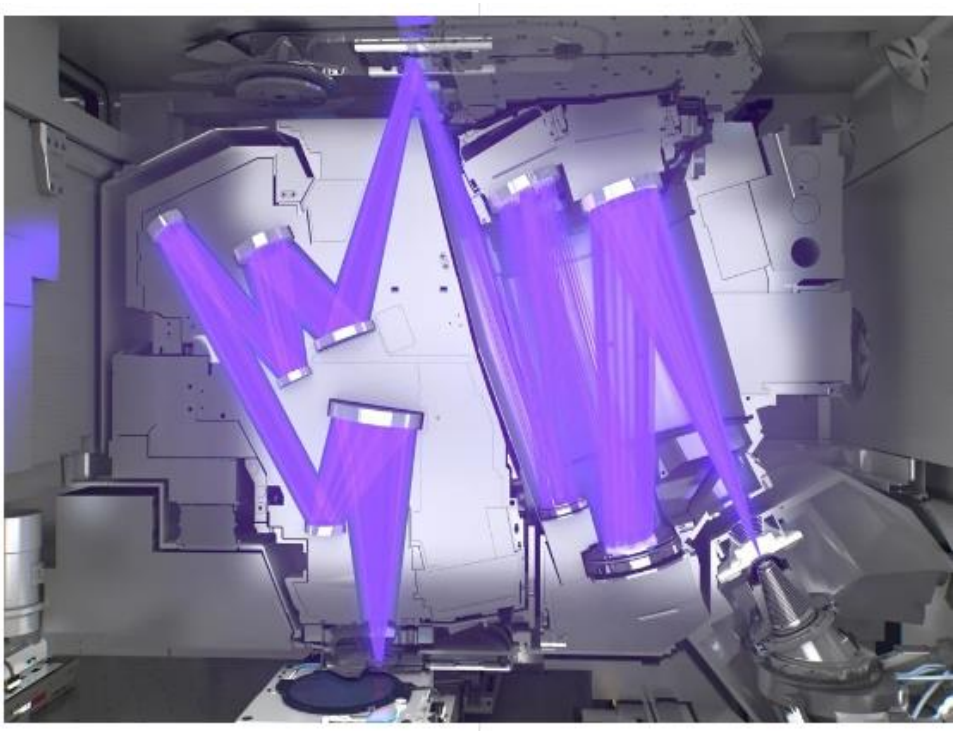

Figure 5 Lithography in EUV machine [1]

Quality is an important parameter for ASML, so understanding thermal contact conduction is critical. Although thermal contact conductance is a complex phenomenon, a slight change at the surface level can make a massive difference for a whole machine.

Figure 5 depicts a UV light source projection through different mirrors instead of the lens, since most materials absorb EUV light, the lenses would absorb the light in the system. The estimation for the heat model is difficult and it generates uncertainty in building the thermal designs. Thus, to minimize heat loss and to generate the best prints, mirrors are used for maximum reflection of the light source even if they are expensive.The main problem in estimating thermal contact conductance is that, at contact pressures above 7MPa [3], the available researched models do not predict the *h'* values accurately. The difference observed between experimental and theoretical values is uncanny.

1.4 Problem definition

As described in the earlier section, for the analyses and prediction of *h'*, a model/tool is required to estimate the range of the thermal contact conductance. However, developing a tool requires a deep understanding of the phenomenon as it depends on several factors. For example, the material and surface properties greatly influence contact conduction. The contact pressure is also the driving factor in determining the h'. It is essential to understand the trend of the contact pressures and heat transfer because due to changes in the applied pressure, the surface encounters deformations, which change the real contact area. Also, it greatly depends on the experimental setup. The sample types and the operator change also introduce uncertainty in contact conductance prediction as well. To develop a model that predicts the *h'*, the first step is to limit the scope of the research.

- ASML's most used materials are aluminium and stainless steel. Thus, the AL5068 variant is selected for starting the analyses. Tin alloy(97/3 Tin-Silver) is later used to identify the effect of deformations by varying contact pressure.
- Two experimental setups are considered for exploring the deformations and contact pressure effects on *h'*
    - One at Philips Engineering Solutions where experiments are performed in vacuum conditions. It is used for measurements on some standardized samples (Al5083).
    - Another in the department of Process and Energy at Technical University of Delft where experiments are performed in atmospheric conditions.
- Use of uniform milled surface samples for symmetry.
- A contact pressure ranges up to 25MPa, as during this regime TCC remains dominant.
- The samples are two flat surfaces with varying roughness for vacuum and a narrow strip of tin for the exploratory study.

1.5 Thesis outline

Chapter 2 explains different factors affecting the thermal contact conductance(TCC) phenomenon. Also, the industrially most used models for TCC estimations are described along with their limitations. Further study is done to identify research questions that will help to resolve the problem step by step.

Chapter 3 explains the experimental setup, which is available at Process and Energy[P&E] department of Technical University Delft. Experiments are performed with tin sample which are later compared with literature models and conclusions are derived. Also, effect of types of deformations on *h'* are analysed and outcomes are discussed.

Chapter 4 explains another test setup available at Philips Engineering Solutions[PES]. Experiments are performed in two campaigns to analyse the effects of contact pressure and *h'* for aluminium samples. Comparison with existing models along with the existing experimental results is done. Also, the effects of aluminium oxide layer effects on *h'* is analysed in campaign 2. Finally, chapter 5 comprise of results and briefly describes the recommendation/future scope on this topic.

2 Literature review

This chapter introduces the reader to the factors affecting thermal contact conduction. Also, this section will discuss the existing estimation models and their limitations. This will help to develop the research objective and specify the direction to proceed.

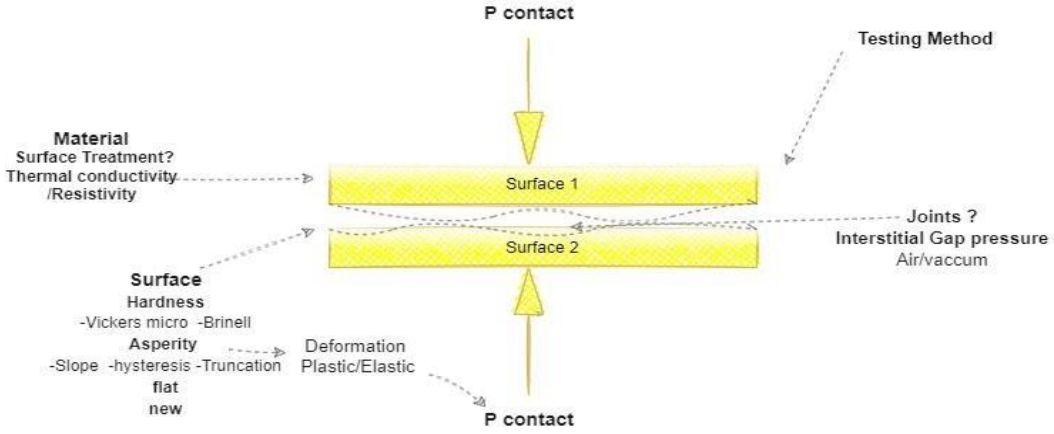

Figure 6 Factors affecting Thermal Contact Conductance

Figure 6 was generated to study the factors affecting calculating the net thermal contact conductance. Starting with the most critical parameter, the contact pressure *p,* which the operator can directly vary. Next are the material properties and surface treatment (milled, turned, smooth). Finally, the thermal conductivity (*k*) is an intrinsic property of the material.

The surface morphology plays a significant role in the calculation. We are considering heat transfer through conduction, which is affected by the asperity slope, roughness parameter (R_a) and microhardness (H_c). The apparatus used for determination also affects estimation.

The atmospheric condition in which the experiment is performed also affects the *h*' value. The experiment can be carried out in a vacuum, in atmospheric air, or in the presence of some other gas. In addition, the samples may have different surface morphology through which the heat transfer is not uniform. Thus, it might lead to inaccuracy in the calculation. Interstitial air gap pressure is developed between the roughness gap of the samples. It does not contribute if the experiment is done in vacuum conditions as there is no air for heat transfer.

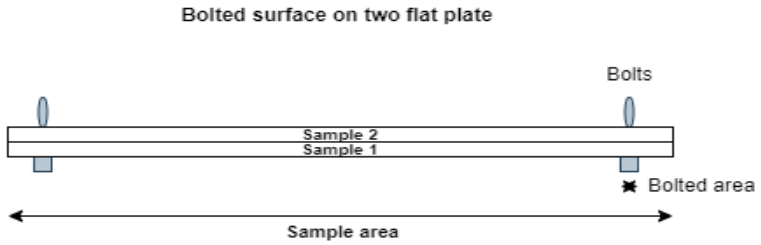

Figure 7 Representation of bolt area to semi-infinite sample

The type of joints (bolted, screwed, hinged) also affects estimation[Figure 7]. To simplify, we consider that the area where bolt or screw are applied is relatively less than the overall specimen or sample area. For simplification we can assume the samples as two infinite flat surfaces in contact, then calculating the heat transfer coefficient on the applied pressure is possible.

2.1 Affecting factors

There are several properties which affect the calculation of contact conductance. Some of the most critical parameters are, [4] [5] [6]

Material Properties:

i. Thermal conductivity of the material (*k*)

It is the measure of conductivity offered by the material. The higher the *k* is, the faster the heat is transferred.

ii. Surface hardness *(*H_v or H_b) and (H_c)

Determined by Vickers($\mathrm{H_v}$) or Brinell hardness ($\mathrm{H_b}$) tests [Appendix B]. It measures how much a material can plastically deform after applying a specific load. Microhardness (H_c) can be defined by the relation to Vickers hardness as [6]

$$\boldsymbol{H_c = 1.08\, H_v} \tag{2.1}$$

iii. Modulus of elasticity (E) and (E')

It is the measure to calculate the resistance to deformity (elastic) for applied stress.

$$\boldsymbol{E = \frac{\sigma}{\varepsilon}} \tag{2.2}$$

Effective modulus of elasticity is the total E of both surfaces in contact and can be calculated by the formula calculated formula [7]

$$\boldsymbol{E' = \frac{E_1 E_2}{E_1 + E_2}} \tag{2.3}$$

iv. Thermal expansion coefficient (α)

The parameter α determines the rate of expansion of material per degree Kelvin.

v. Geometric properties of the contacting surface, roughness, asperity slope.

Surface roughness is defined as the irregularity that develops due to production processes like milling, turning, etc. A rougher surface means more abrasions or large deviations in spacing. Asperity slope is a property of the surface's crests and troughs formed due to roughness and surface operations.

Process Factors :

vi. Contact pressure (*p*)

It is the applied pressure on two surfaces in contact and is usually known in most test apparatus.

vii. Mean temperature (T_m)

The average temperature between two surfaces is the mean temperature.

2.2 Existing models

The existing models use some relations developed by previous factors for two surfaces in contact, this section will discuss the probable relations and calculations.

As from [2], the thermal resistance in series follows an inverse relationship in calculating mean conductivity.

- For two materials in contact, their mean conductivity can be taken as.

$$\boldsymbol{k} = \frac{\boldsymbol{2k_1k_2}}{\boldsymbol{k_1 + k_2}} \tag{2.4}$$

- Roughness parameters can be defined as Ra, which is arithmetic average of roughness throughout the material area of consideration and abides by formula.

$$\boldsymbol{R_a} = \frac{\boldsymbol{1}}{\boldsymbol{L}} \int_{\boldsymbol{0}}^{\boldsymbol{L}} |\boldsymbol{y(x)}| \boldsymbol{dx} \tag{2.5}$$

Here, L is the total length trace of the surface and Y(x) is the distance from surface's mean plane.

- Standard deviation for roughness parameter is σ that is root mean square roughness and follows the equation.

$$\boldsymbol{\sigma} = \sqrt{\int_{\boldsymbol{0}}^{\boldsymbol{L}} \boldsymbol{y(x)^2 dx}} \tag{2.6}$$

- Another parameter which is mostly used after R_a is R_z. Figure7 represent a surface with length L, divided into L_1 and L_2 according to the asperity slope peaks which have 10 peaks and dips. R_z is calculated by averaging the vertical distances between the highest peak and the lowest valley over a five asperity peak for one period. R_z averages only the five highest peaks and five deepest valleys, so extremes have a much greater impact on the final value. Figure 8, the R_z varies after every 5 consecutive crests. $R_{z1}$is the distance between highest peak and lowest dip in 5 consecutive asperity slopes and similarly for R_{z2}.

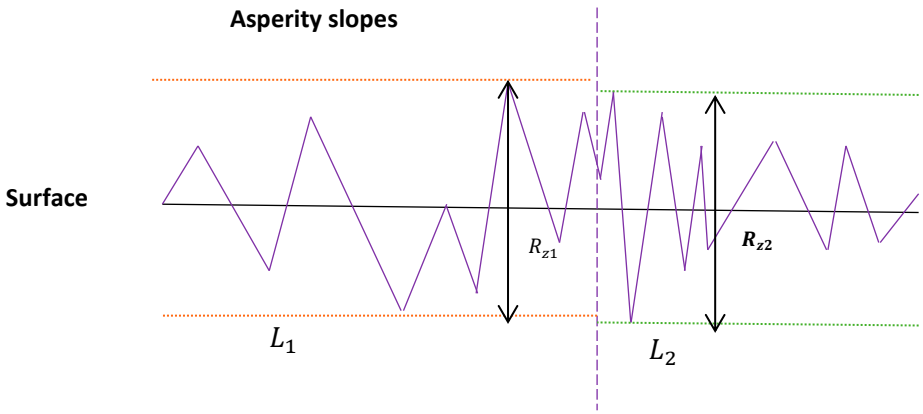

Figure 8 Roughness Calculation method(Rz)

The surface R_z is the average of individual surface parameters and can be calculated as,

$$\boldsymbol{R_z = \frac{(R_{z1} + R_{z2})}{2}}$$

Out of R_a and R_z only one should be considered for any type of calculations to avoid confusion.

- Asperity slopes are important property and it largely determine the elasticity of the material, small slopes will make the material more elastic and to sustain more force. Whereas sharp slopes might break during applying pressure and tend to make material deform plastically. Asperity can be defined as unevenness of the surface or ruggedness. When two surfaces are in contact, they touch only few asperity points .When materials are touching at only few asperity points, the actual contact area is very less than the total contact area. Thus, it reduces conduction heat transfer.

  It follows the same relation with the roughness parameter from [4], *m* is the absolute average asperity slope. *m'* is the root mean square of the asperity slope. They are related accordingly as [7].

$$\boldsymbol{m' = m\sqrt{\pi/2}} \qquad (2.7)$$

It can approximately be taken as *m'=1.25m*. The effective mean square for roughness and mean slope of asperity can be expressed as

$$\boldsymbol{m = \sqrt{{m_1}^2 + {m_2}^2}} \quad \text{and} \quad \boldsymbol{\sigma = \sqrt{{\sigma_1}^2 + {\sigma_2}^2}} \qquad (2.8)$$

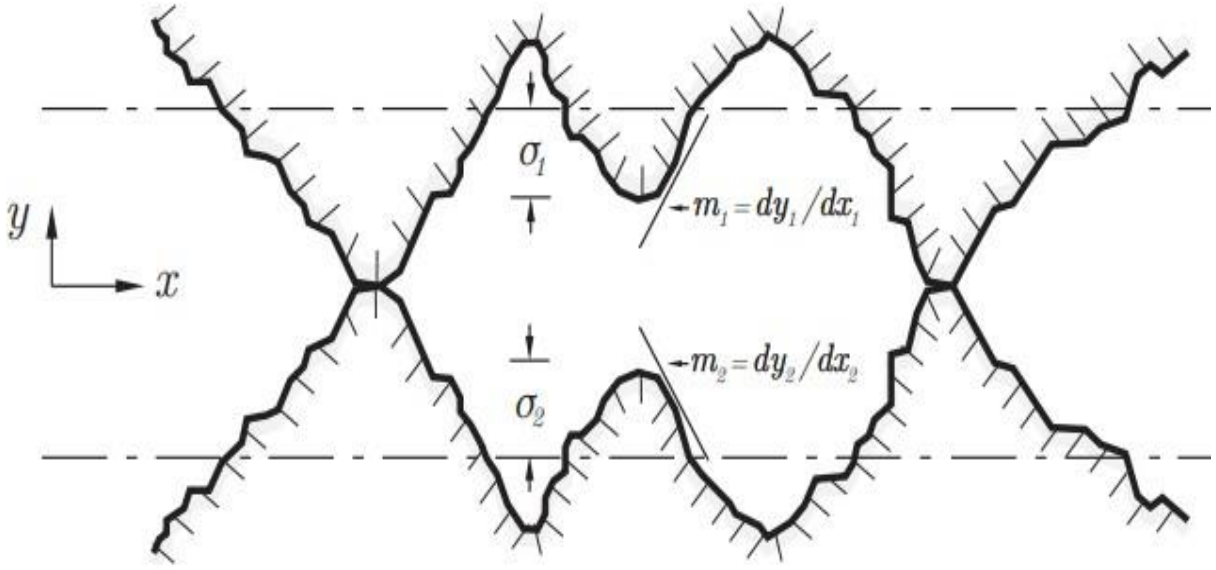

Figure 9 Two surfaces in contact showing asperities of absolute surface slope m and root mean square roughness [4].

2.2.1 Types of deformation and models

There are two types of deformation possible when the pressure is applied: elastic and plastic deformations. An elastic region is where the deformity can gain back its natural properties when the pressure is removed. Plastic deformation is permanent and cannot be reversed completely even after the pressure is removed and the deformation is permanent.

When the Pressure is just applied, the linear elastic deformation starts. At the limit of proportionality deformation becomes nonlinear elastic. Increasing the load more than a materials' yield Strength, the permanent deformation starts and that lands in the plastic region. After a certain measure of applied strain there is fracture point where the material finally breaks(cracks). As the heat conduction depends directly on the contact area, it will be lower in elastic deformation but since the contact increases with plastic deformation, conduction increases.

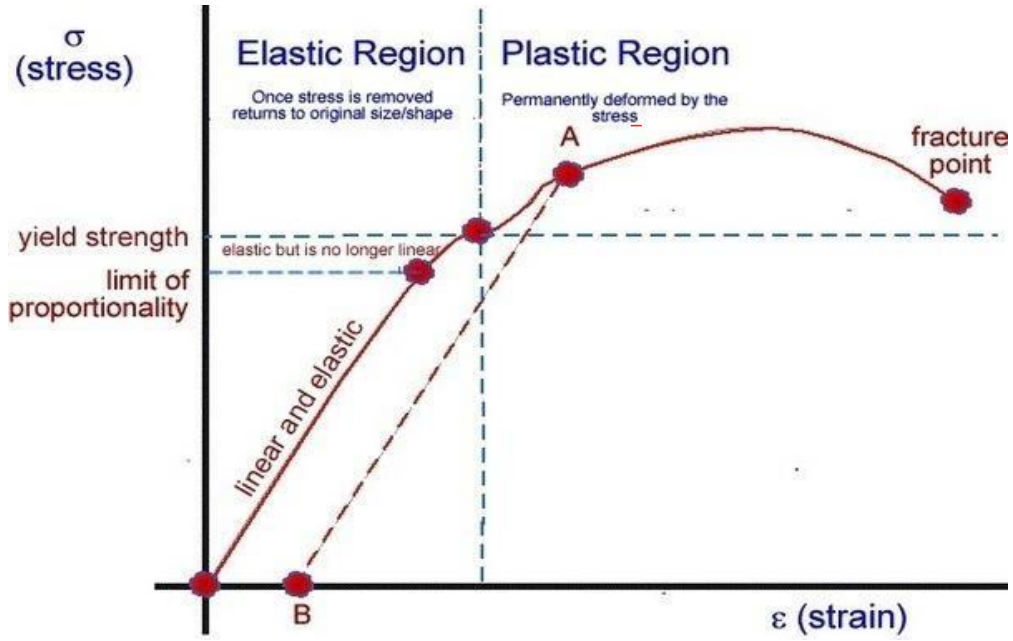

Figure 10 Stress vs Strain deformation curve

Thus, it is very essential to know the deformation type to understand the reproducibility of experiments. The type of deformation (elastic or plastic) of these roughness peaks plays a vital role in the type of microcontact. Moreover, has a significant effect on the thermal contact conductance value. Elastic deformation results in much lower thermal contact conductance than plastic deformation. Mikic [8] developed a model to determine the type of deformations.

Here,

$$\gamma = Hc/(m'E') \quad (2.9)$$

γ=dimensionless parameter

E'=effective modulus of elasticity

H_c= Microhardness, and

m' = root mean square of the asperity slope

The main conclusion derived in this specific research is that "Deformation would be predominantly

elastic for $\gamma \geq 3$ and predominantly plastic for $\gamma < 0.33$"[15]. Based on this, two models for thermal contact resistance were developed. The deformations due to loading and its effects are later studied in Chapter 3 methodology while performing experiments with tin sample in the university.

2.2.1.1 Contact conductance by Elastic deformation ($\gamma > 3$)-Mikic [8]

The basic phenomenon of contact conductive heat transfer was understood by 1973, but there were not many significant contributions toward identifying the effects of surface behaviour in contact. For example, if the deformations of asperities are elastic, the thermal resistance prediction is difficult. Furthermore, not much analyses was done for the deformation of asperity slopes.

The calculations of samples are considered as two flat surfaces in contact. The model was developed to understand the contact conduction, considering surface effects. Mikic [7] developed an equation to predict the nature of *h'* with respect to many factors, including surface properties.

$$h' = \frac{1.55 m' k_m}{\sigma'} \left(\frac{p\sqrt{2}}{E' m'} \right)^{0.94} \tag{2.10}$$

$$h' = 2.83 k_m \left(R_a^{-0.955} \right) \left(\frac{p}{Hc} \right)^{0.94} \tag{2.11}$$

h' = thermal contact heat transfer coefficient [W/(m^2 ·K)]

k_m =mean thermal conductivity of the interface [W/(m·K)]

m' = effective mean of the absolute slope of surface profile [rad]

σ' = equivalent RMS surface roughness [m]

R_a = Roughness parameter [µm]

The derivation of this equation uses the Hertzian theory [11] that the plastic region's thermal contact area is twice that of the elastic.

Also, the contact pressure for elastic deformation p_e can be represented as

$$p_e = \frac{p\sqrt{2}}{E' m'} \tag{2.12}$$

2.2.1.2 Contact conductance by Plastic deformation ($\gamma < 0.33$) – Yovanovich [9]

After the proposal of Mikic, further research was done by Yovanovich to analyze plastic deformation. The model was developed specifically for plastic deformation of the asperities. The basic mathematics was involved in deriving the final equation and can be traced back to a section of a journal by Yovanovich [13].
The equations are,

$$h' = 1.25\frac{m' k_m}{\sigma'}\left(\frac{p}{H_c}\right)^{0.95} \tag{2.13}$$

$$h' = 4.2 k_m \left(R_a^{-0.257}\right)\left(\frac{p}{H_c}\right)^{0.95} \tag{2.14}$$

Although these best-fit parameters are used for prediction, they have limitations. Working under vacuum conditions, extra unknown factors to consider if the surrounding is an atmosphere or any other.

- Yovanvich and Mikic model works only for low pressure, up to 7MPa. [3][10]
- It considers apparent contact pressure, for which determining the exact surface in contact seems not practical as it changes with pressure applied

2.2.2 FVV (Forschungs Vereinigung Verbrennungskraftmaschinen) [3]

FVV is Research Association for combustion engines in Germany(Fankfurt). The research was conducted in RWTH Aachen and later documented.

For internal combustion engines, there was a need to calculate the thermal contact conductance for high contact pressures up to 200MPa. Unfortunately, the available theoretical models (Yovanovich, Mikic, Lambert and Fletcher) are for steel and are not reliable anymore beyond contact pressures of 7MPa. Also, they are not accurate to predict the range. Thus, the empirical relation was made by developing an experimental setup and performing experiments.

All the experiments were done under atmospheric conditions(1 bar pressure), which implies the air-filled interstitial gaps. Here, no filler materials are considered between the contact surfaces. An empirical model aluminiumpressures. This model is only for materials stainless steel and aluminium which are used in internal combustion engines.

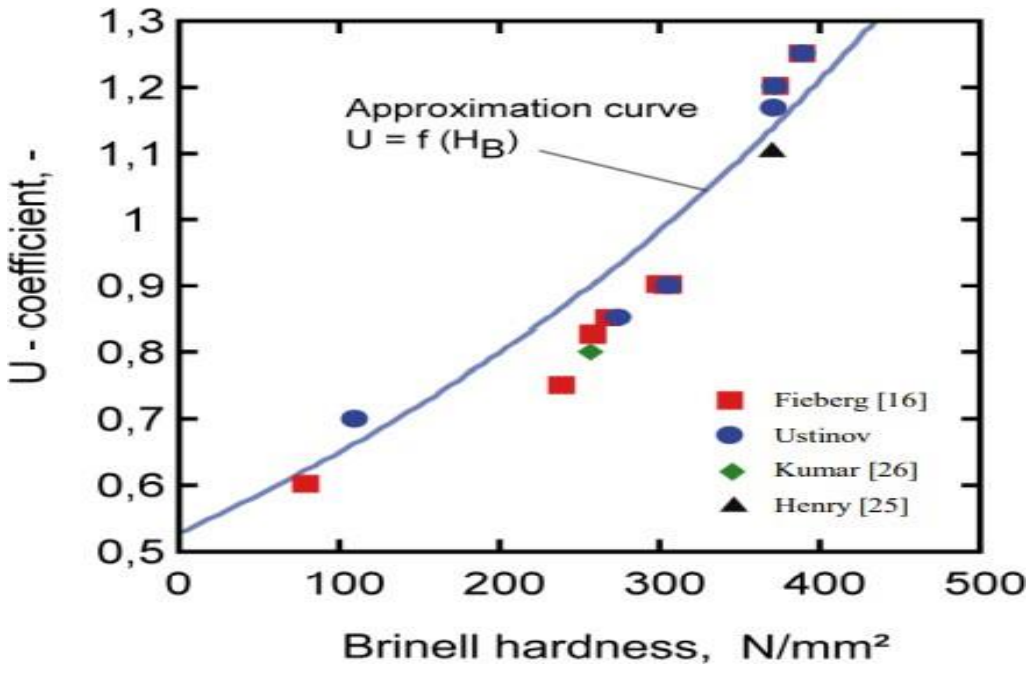

Figure 11 Brinell hardness and U [3]

It consists of two empirical relations, which include the variable *U*. *U* is a function of Brinell hardness, and its dependence is studied by the experimental results curve slope and is explained by the graph. It can be stated as the empirical dimensionless number. The range of Brinell hardness [Appendix B] in this experiment was varied. [aluminium alloys H_b=80MPa to steel alloys H_b =400MPa]

Figure11 explains the graph to determine the *U* for the Brinell hardness. Ustinov in a blue dot is the result found by the experiment for which the *U* function curve is fitted as a function of Brinell hardness. Different model results were compared and plotted in the same graph to understand the trend. It seems most of them lie close to the trend developed and are in good order to predict the *U* function for the calculations of *h*'.

Using the same function *U,* two empirical relations are developed for two materials, stainless steel and aluminium. Although the relations are quite similar, there is a change in power. The explanation for a change of power is that it is an empirical relation that was altered according to the experimental results. The change was made for aluminium to develop similar and correlating empirical relations.

1 Stainless Steel

$$\boldsymbol{h' = C\left(\frac{k_s}{\sigma'}\right)\left(\frac{p}{H_b}.U(H_b)\right)^{\sqrt{\frac{po}{p}}}} \tag{2.15}$$

2 Aluminium

$$\boldsymbol{h' = C\left(\frac{k_s}{\sigma'}\right)\left(\frac{p}{H_b}.U(H_b)\right)^{10\sqrt{\frac{po}{p}}}} \tag{2.16}$$

Here,
C=0.008 Experimentally determined constant
Hb = Brinell Hardness [MPa]
$\sigma'=(R_{z1}+R_{z2})/(R_{z1}R_{z2})$ [m]
P0 = 1 [MPa] Nominal contact pressure

The empirical relation was made for the materials used in the IC Engine industry. There was a vast difference between the trend of *h'* for steel and aluminium. A similar empirical relation was developed but with changing the dependence of *h*' on applied contact pressure as aluminium will start plastic deformation very fast as it has low hardness and malleability.

Another observation in the relationship can be that as the pressure increases, the power decreases, which might lead to less increase in overall *h*'. At the start, *h'* rises quickly with increasing pressure, but after a particular time, the *h*' increment concerning pressure is relatively steady.

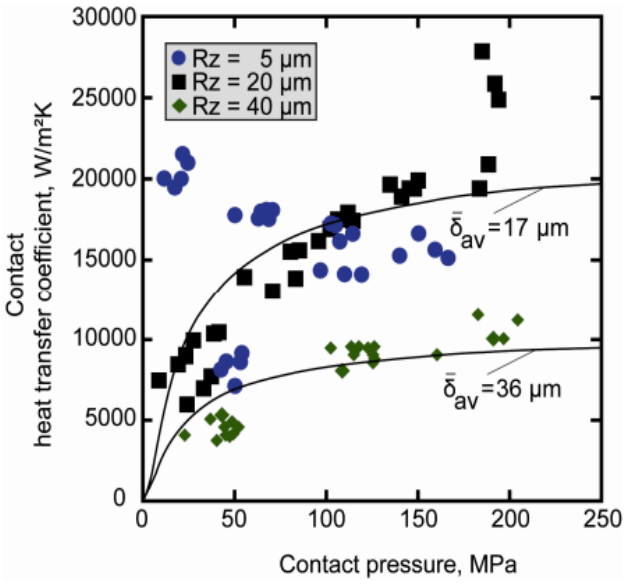

Figure 12(a) Steel empirical relation curve [3]

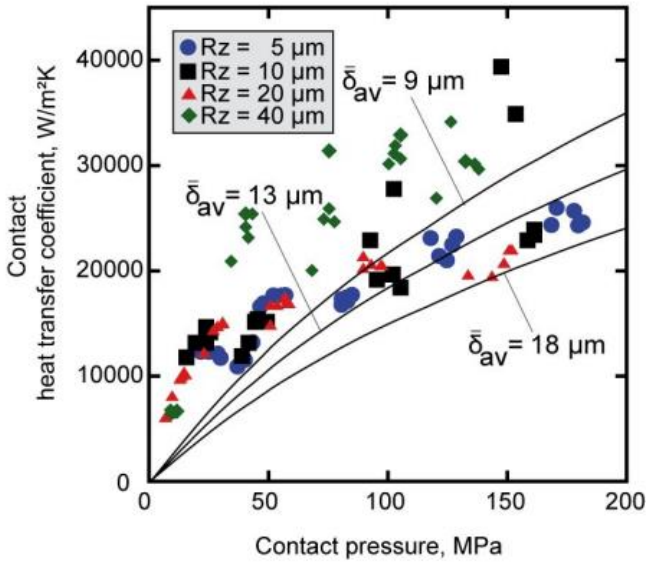

Figure 12(b) Aluminium empirical relation curve [3]

Figure 12[3] plots experimental *h'* values with different roughness values. The solid lines depict the empirical relation prediction throughout the roughness. As the empirical relation is dependent on roughness, it has a different prediction line for each roughness.

For steel, It can be seen that the increase in *h'* value at the start is way more than after 100MPa. The region around 200 and later is called a steady state as the *h*' is constant. For aluminium, the predictive curve is not linear but a little different. Nevertheless, the predictions are in good order with the experimental results, and the previous paragraph's observation is also compatible with physical understanding.

The model is quite acceptable in industries, and ASML is also used to predict the *h*' range at higher pressures. But there are some constraints of the FVV model,

- The model was developed with several experiments performed on aluminium and steel samples but *h'* of materials with known brinell hardnesses may be estimated.
- It cannot include other gas parameters than the atmosphere, whereas we use vacuum environment in EUV machines.
- This model does not work for low pressure or elastic deformation region, as meant for IC engine industry.
- The different setups might have different errors which are difficult to predict. Calculating uncertainties in prediction are complex as there are several variable sources inducing uncertainties.

2.3 Research Questions

After the literature survey, this section aims to find a correlation between different models. It aims to understand the trend of *h'* by different factors.

The theoretical models are not helpful for the accurate prediction of *h'*. The pressure range is not feasible to use in industries. Also, the roughness parameter has a different relationship with Mikic and Yovanovich. There might be different factors affecting *h'*, which have not been accounted for yet. No

proper surface factors are considered which might describe the behaviour of *h'*. There is a need to analyse more to find the research objective. The FVV model is more like an empirical relation and material specific.

The main conclusion after the literature study can be drawn by formulating the research objective. It can be depicted as,

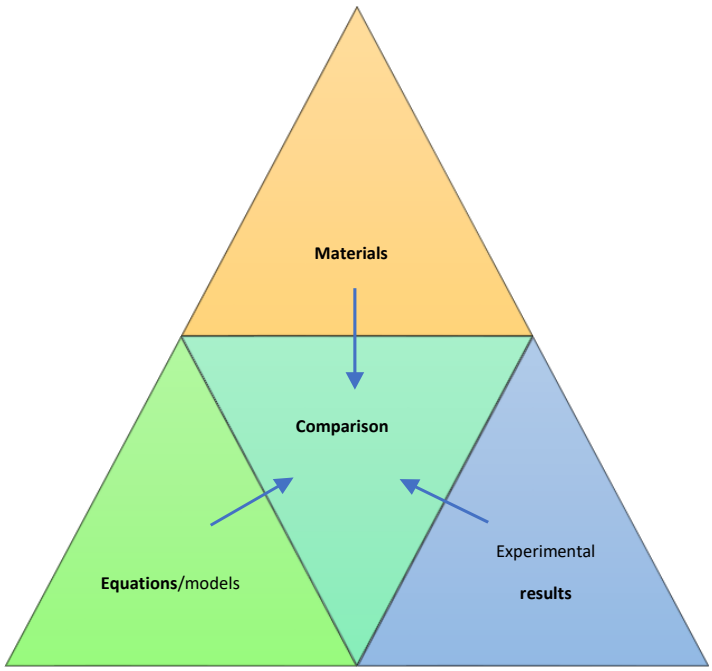

Figure 13 Comparison for defining research objective

Firstly, for starting the research, the most used materials in the literature previously and in the industry are considered. Then for deep understanding we compile all the previous models with their theoretical/empirical relations specific to material type or surface properties. Later, the comparison of experimental results which are available in the research domain is done. All of the models have a standard solution to compare each aspect to generate the required research and sub-research question. Primarily some comparisons are developed for generating the final objective to be answered at the end of the thesis. Sub-research questions will help to achieve the end result step by step.

2.3.1 Sub Researchquestions

Starting the analyses with considering one of the useful paper, Baharami [10]. It focuses on calculating thermal contact conductance(*h'*) in a vacuum for nickel coated(6µm) aluminium surfaces. The nickel coating is very thin and is required to prevent damage to aluminium surface as aluminium reacts with atmosphere to form aluminium oxide. The cylinder joint experimental setup is used[Appendix D].

It compares their experimental data to some available models to predict thermal contact conductance for both elastic and plastic deformation. Figure 14 plots the experimental results with Yovanovich and Mikic outside their working regime to motivate the first sub-research question. As we observe that Yovanovich(plastic) is overpredicting but with similar slope rather than Mikic. Proposed outcome from this paper is that we should focus on plastic deformation for micro-contacts.

Thus, the first sub-research question arises, **"Identify the need to develop a whole new model for *h'* prediction and its feasibility ".**

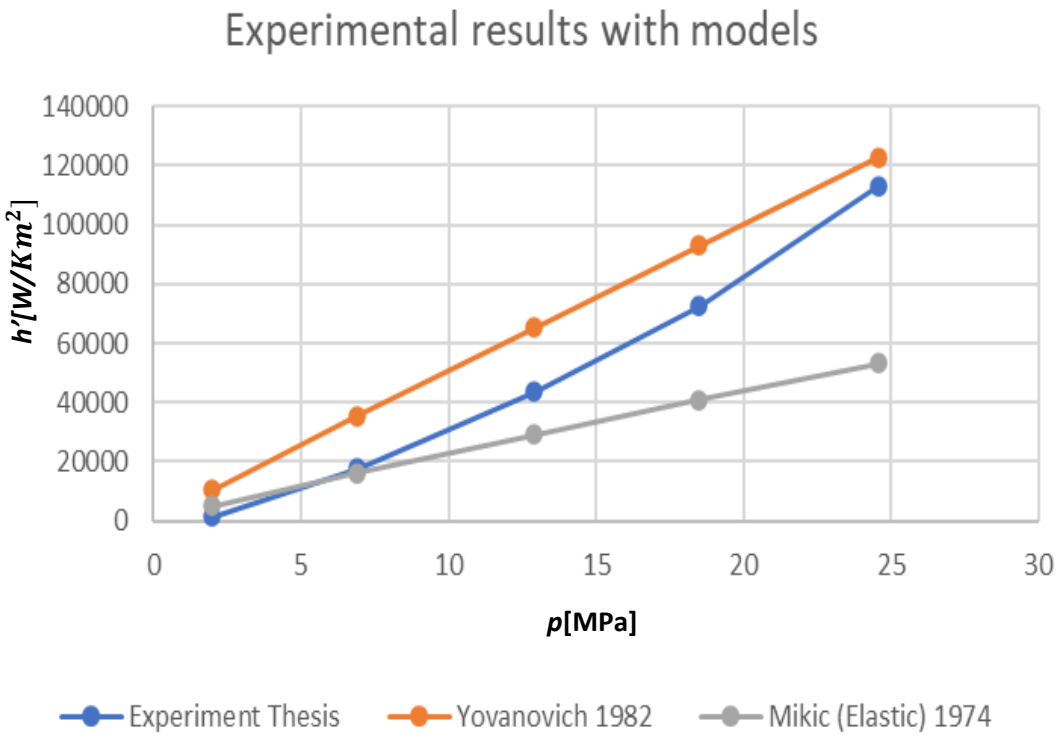

Figure 14 Models prediction with experiment[14]

Graphs are plotted where it seems Mikic is underpredicting and Yovanovich is overpredicting. Also, the Mikic parameter(γ) is less than 3.Thus, the deformation is expected to be in the elastic region, and the experimental results should follow the Mikic equation but are not following. It can be observed that the Mikic equation is not dependent on Macro/Microhardness. Therefore, it might be a cause for the underprediction.

The determination of the equation might be because of different materials or the different pressure ranges. Therefore, checking the possibility that we can choose any of the reference equations is important for developing a new relation and defining trend oh *h'* with the variables. The reference or base equation can be described as existing model equation, where we would want to tune/readjust certain parameters that effects *h'*. There might be a need of introducing new parameters or changing the relation with existing parameters for developing an semi-empirical relation.

This comparison directs to another vital question that should be answered: "**Equation/model can be taken as reference equation to form the empirical relation**".

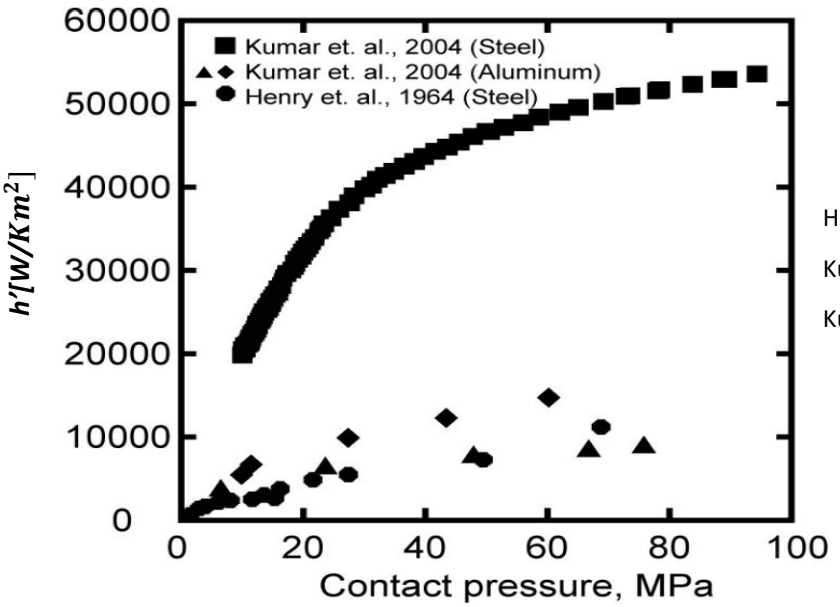

Henry steel(R_a =1.5 µm)

Kumar aluminum(R_a = 1.5 µm)

Kumar steel(R_q = 3.04 µm)

Figure 15 h' vs pressure for different materials [11]

Figure 15 represents a graph between contact heat transfer coefficient and contact pressure for steel. It was compared with similar material's experimental results in paper from 1964[16]. The significant observation is that only the roughness parameter has changed from R_a 0.5µm to R_q 3.04 µm, and the graph has altered. Whereas the aluminium has same trend with different roughness. There is unknown relation of both roughness types but one speculation can be that for steel curves, they both follow a similar curve trend. On the other hand, the aluminium material has no similarity in any aspect except the trend. Which leads to another question: "**Does change in materials always alters the equation? Which material properties effects most?**"

While observing the trend in Figure 16, the infrared thermography [Appendix D]type of experiment was performed [12] [13], where the heat flux was calculated, and the heat transfer coefficient was calculated. Then the graph between the conductance heat transfer coefficient and the contact pressure is plotted for different heater temperatures of 300°C and 200°C. The material taken is N1019 steel(Steady state equipment).

As for 300°C, there is a change in slopes of the curve on specific points of the different roughness, that is, for R_a value 0.45µm (nearly smooth surface). The trend changes completely at around 115MPa. Similarly, there are noticeable critical points for each roughness and changing the central input heater temperature.

It develops another question: "**Identifying reason behind a change in slope after certain pressure in prediction of *h'*.**"

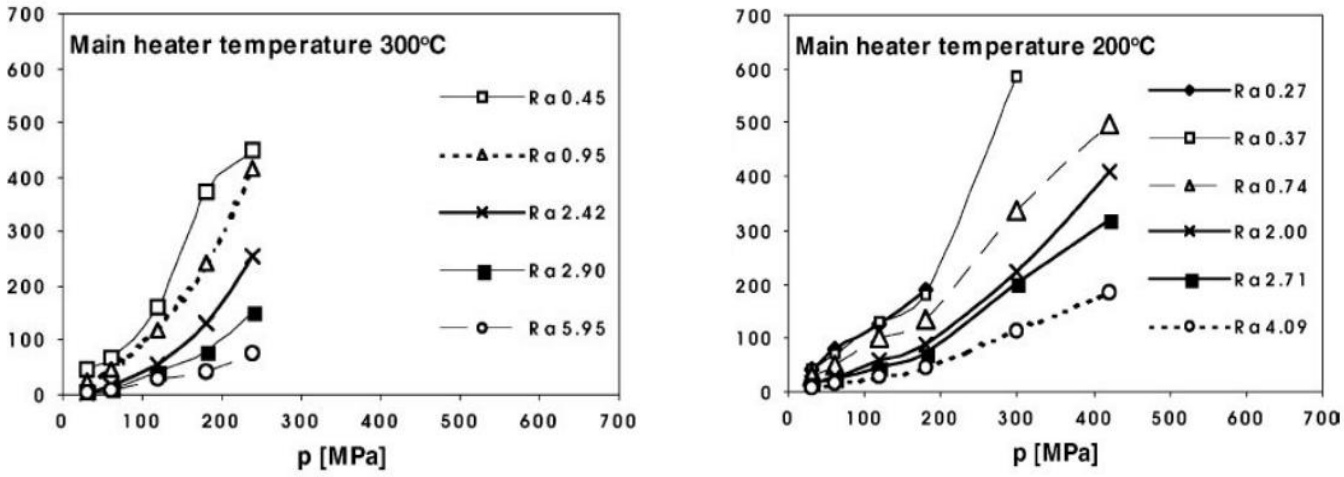

Figure 16 Contact conductance variation with roughness [15] [3]

For changing materials, at least one parameter must drive the change significantly. Also, the reason behind the critical point is yet to be determined. Moreover, a hypothesis can be that in the start, when the contact pressure is low, the deformation is elastic. When the pressure is further increased, the plastic deformation is started and the slope is changed.

This might be one of the probable causes, so there is a need to justify the reason by physics. There is a need to select the best possible procedure to make the model feasible in terms of accuracy and acceptance of the physical "Real "usage. The last objective is,"**Method to fit data for correlation (curve fitting, randomization, data analyses ,or some other methods)**?"

Another important aspect is uncertainty analyses, there are several sources of uncertainty that are stated as,

Error type – Systematic, Random, Experimental and others.

Different apparatuses can induce different uncertainties. Some of them are,

- Cylinder Joint experiment [Appendix C]
- Infrared thermography [Appendix D]
- TU Delft setup [Chapter 3]
- Philips test setup [Chapter 4]

The type of surroundings might lead to different uncertainties. Whether it is vacuum, atmosphere or any other gas, it will affect the h' determination. Although most errors cannot be omitted, some can be reduced. Systematic error can be reduced by randomization, and Experimental error can be reduced by standardization. The calculation of total uncertainty is quite tricky to estimate.

An error that best fits should be assumed. Assumption needs to be supported with practical reasons and evidence. For estimation, there were comparisons of error range of some apparatus that are taken.

- Experimental setup in Philips, Eindhoven

The uncertainty range is 20% for samples with the area of 50mm^2,tests are performed in a vacuum.

- Apparatus in TU Delft, Delft

Claims approximate error range of 35% for aluminium and steel samples. Tests are performed under atmospheric pressure. To simplify, an assumption was made to consider the net error slab in the model development to be 20% in each aluminium and stainless-steel material in a vacuum. **Error! R eference source not found.**Figure 17 shows that the *h'* value can be anywhere between the defined error bars and the whole range where *h'* can lie. It increases the complexity of predicting *h*' accurately.

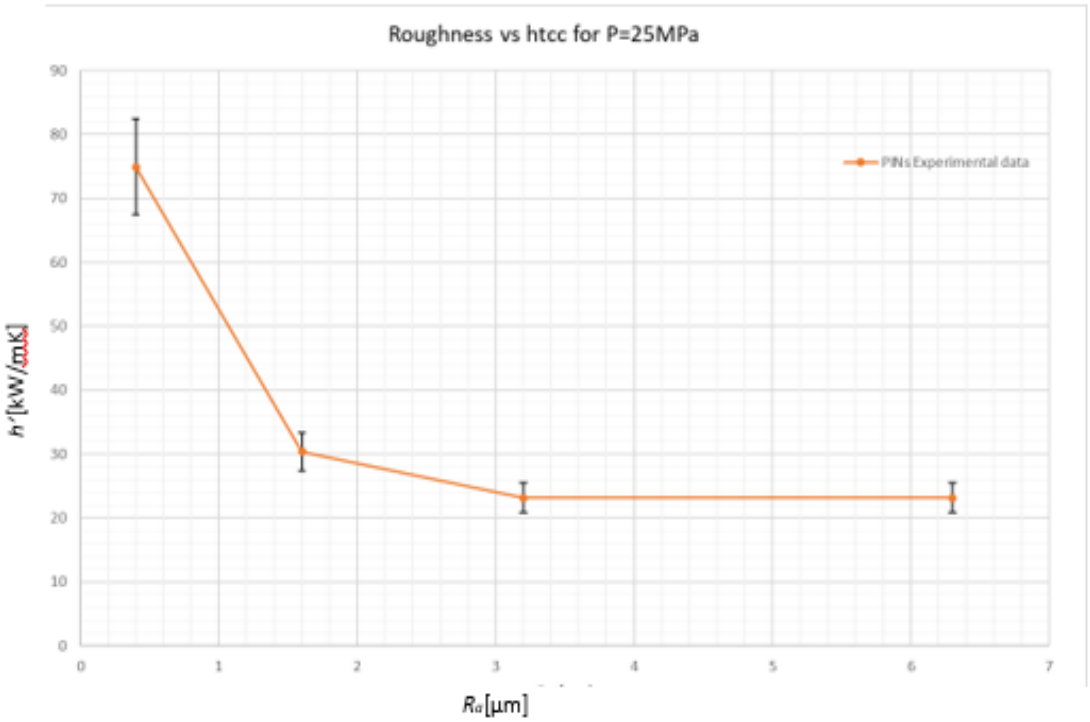

Figure 17 Range of h' for experimental value from PINs

An important conclusion is that estimating the exact heat transfer coefficient is not possible. However, estimating the range of *h'* for a specific apparatus and material may be possible. This comparison summarises all the research objectives to be analysed and solved by the end of the thesis research.

1. **Identify the need to develop a whole new model for *h'* prediction and its feasibility.**
2. **What Equation or which model can be taken as a reference equation to form the empirical relation?**
3. **Does change in materials alters the TCC prediction? If so,which material properties effects most?**
4. **To Identify the reason behind the change in slope after certain pressure in prediction of TCC'**.
5. **To identify best method to fit data for correlation (curve fitting, randomization, data analyses or some other methods).**

The idea is to develop a model while taking a reference equation or correlating the previous equations that keep the physical relation intact. Defining a material and its intrinsic properties is essential, as heat transfer is highly dependent on it. The fitting is usually taken as best fit according to the relation some specific experimental data set holds and depends on the apparatus.

All these questions serve as step-by-step approach to reach the final problem definition discussed in the next section.

2.3.2 Final Problem goal

Our goals can be summarised as follows:

- To understand the thermal contact conductance coefficient(*h'*) dependence with type of deformations and contact pressure.
- Comparing the prediction of *h'* from available models(Mikic, Yovanovich and FVV) to experimental results.
- And, to develope a semi empirical formula to predict *h'*.

3 Experimental Methodology(i)

This chapter deals with understanding the deformation effects on heat transfer, it consists of a hypothesis, and experiments are performed on the TU Delft setup in the P&E department. When two metal surfaces are in contact, heat transfer taking place through the contact is dominated by conduction. Under different contact pressures, there will be a different amount of heat transfer. The major reason for this is the change in surface geometry while applying variable pressure. The surface deformation can be elastic or plastic, depending on different factors like modulus of elasticity, yield strength of the material, geometry of surfaces in contact and applied pressure.

Hypothesis:

If increasing load pressure results in increase in the contact conductance, which stays within the elastic range of deformation, then decreasing the load pressure should proportionally decrease contact conductance. Alternatively, if the plastic deformation limit is reached at surface locations, after unloading it should not result in decreased contact conductance at previous contact pressures as the effective contact area has increased.

The following model experiment will verify the claim:

Clamping a soft material with a specified geometry, such as tin, between two smooth copper surfaces simulates the impact of the rough surface. Since thermal conductivity, young's modulus and Brinell hardness of copper are all high, neither the copper's surface indentation nor the material's deformation will have a substantial impact on the copper's ability to transfer heat. The experiments here are performed with a sample taken as plain round tin bars of 2mm diameter(soldering tin wire).

Experimental Setup:

This test setup(GUNT WL374) is used[Figure 18] for determining the temperature difference between two surfaces. With this setup, the *h'* value can be determined. The major components of the test setup are,

- Electric power connections: The electrical power supply is used for the heater to run. Ammeter and voltmeter are used to measure the power applied to the heater. The display is used to note the sensors' temperatures.
- Temperature sensors: Thermocouples are placed in 5 locations of sample arrangement, and the sixth measures water temperature.
- Water pump connections: It is used to :
    - To keep the sample base at a constant temperature, the water cooler supplies constant water flow.
    - To maintain the water cooler's flow rate and regulate if water overflows. A water pressure regulating tank is used for this purpose.
- Support: consists of screws and bolts to keep stacked samples in place and an aluminium shield on top to reduce loss by radiation.
- Heater and Samples: The heater and samples have a cylindrical shape. The heater is made of copper, the sample material taken here is tin wire.
- Isolation cylinder: The cylinder is placed over the top of the whole arrangement and is used to reduce heat losses.

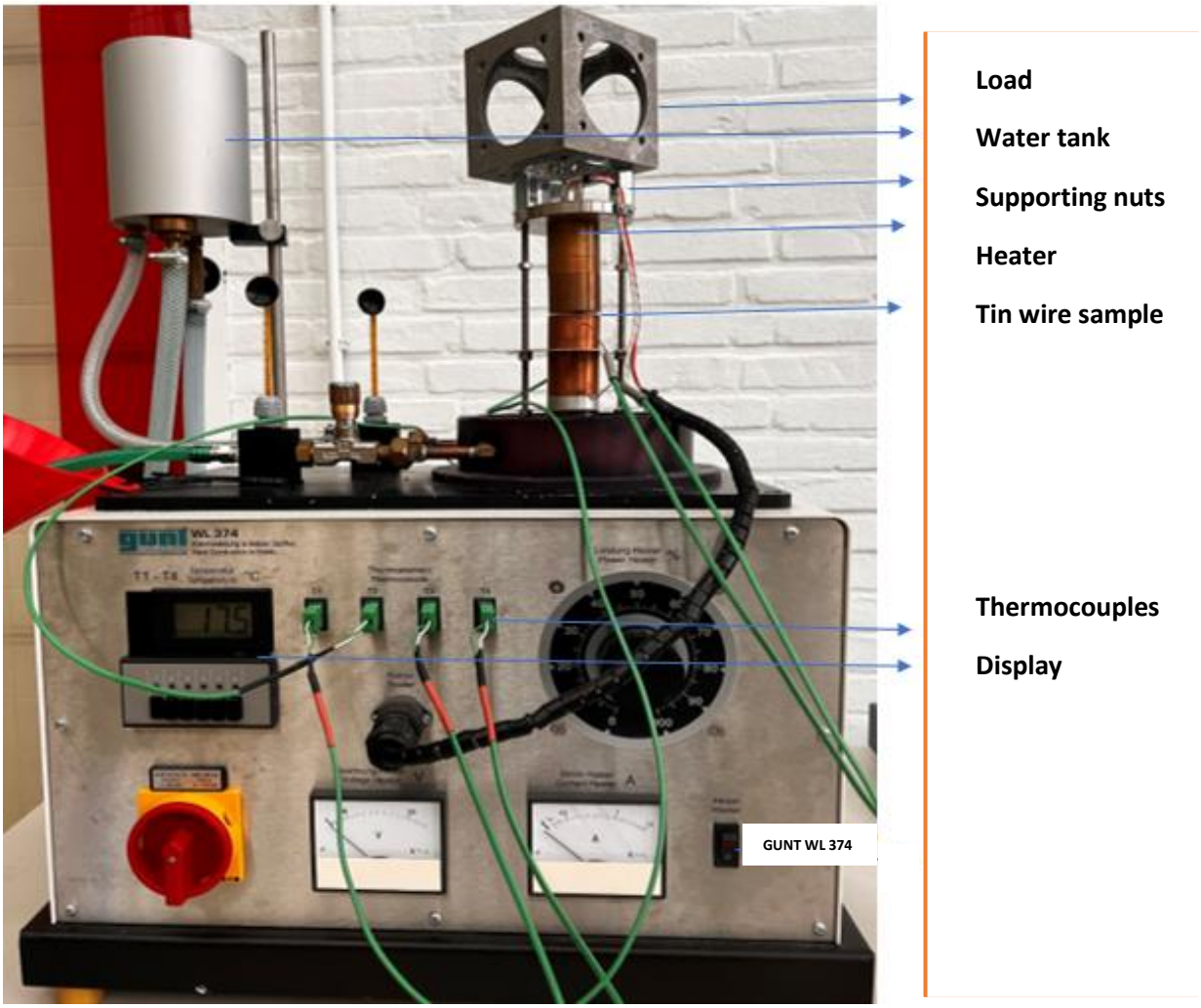

Figure 18 TU Delft Setup(P&E)

The test procedure:

The samples initially were copper cylinders with diameters of 40mm each with different lengths. A copper heater is placed on top of aligned samples and the bottom is kept at a constant temperature by tubes with flowing water.

The heater is turned on and after some time when the setup reaches steady state then the temperature difference is used to determine *h*'. Each sample has the same cross-sectional area. The samples are stacked and placed aligning with the heater, as shown in Figure 21. Thermocouples are placed inside the holes drilled in the samples to analyse the temperature profile.

When water cooler is on and the flow is constant, 50% power(110V) is supplied to the heater. The readings are logged manually every 2 minutes for an hour until a steady state is attained. The

temperature readings are used to find the effective heat transfer coefficient(*h*') at the samples' contact.

The experiments are first performed to find the thermal conductivity of copper cylinders. For this, the tests are performed with no contact pressure and with the isolation cylinder covering the test section.

There were some experiments performed to determine the conductivity of copper cylinders which are to be used later with tin sample. As both the cylinders are made of copper we expect to have similar conductivities on top and bottom cylinder. For this we calculated the conductivity of copper (k_{cu}) as a mean of conductivity of both copper cylinders which is averaged over three experiments. From figure 21, $L_1 = 30\text{mm}$ and $L_2 = 60\text{mm}$, are used to calculate the conductivities with formula,

$$\boldsymbol{k = \frac{Q * L}{A * (T_1 - T_2)}} \qquad (3.1)$$

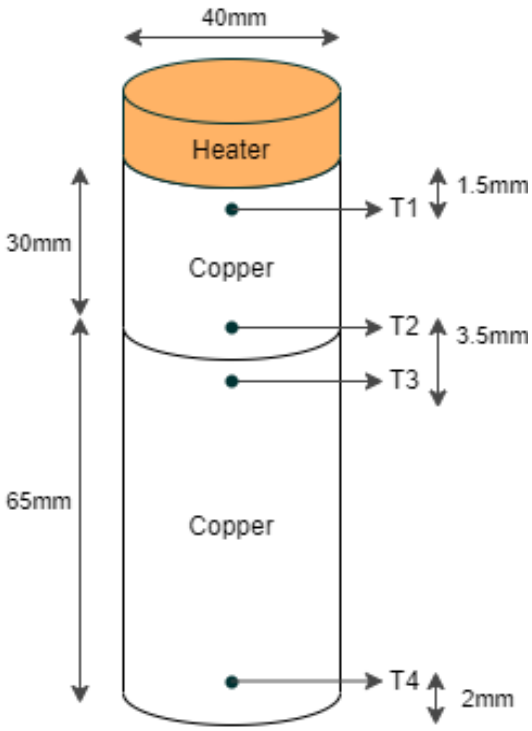

Figure 19 Sample arrangement

The average conductivity of copper (k_{cu}) was found to be 433.75 W/mK. This conductivity will be used later to estimate heat conduction with a rough surface in between the cylinders.

Experiment No.	Power supplied *Q=VI*	$k_{top} = QL_1/(T_1 - T_2)A$	$k_{bottom} = QL_2/(T_3 - T_4)A$	k'_{cu}	k_{cu}
	[Watts]	[Watt/mK]			
1	70 [40%]	433.56	429.19	431.38	
2	106 [50%]	436.99	433.24	435.12	**433.75**
3	152 [60%]	437.03	432.46	434.75	

Table 1 Thermal conductivity of copper cylinders

To understand the heat transfer in depth, a thermal resistance model is made and later the experimental results are compared with the outcomes from Yovanovich and Mikic models.

Model for thermal Resistance:

To understand the resistance offered by the tin wire when implementing the sample between copper cylinders, Figure 29 depicts the thermal resistance model. The simplification of a circular wire can be done by assuming it to be a rectangle(grey) of equal area that is $\pi r^2 = (2r)h_3$ which gives the height of the rectangle $h_3 = \pi r/2$ that is 1.57mm.

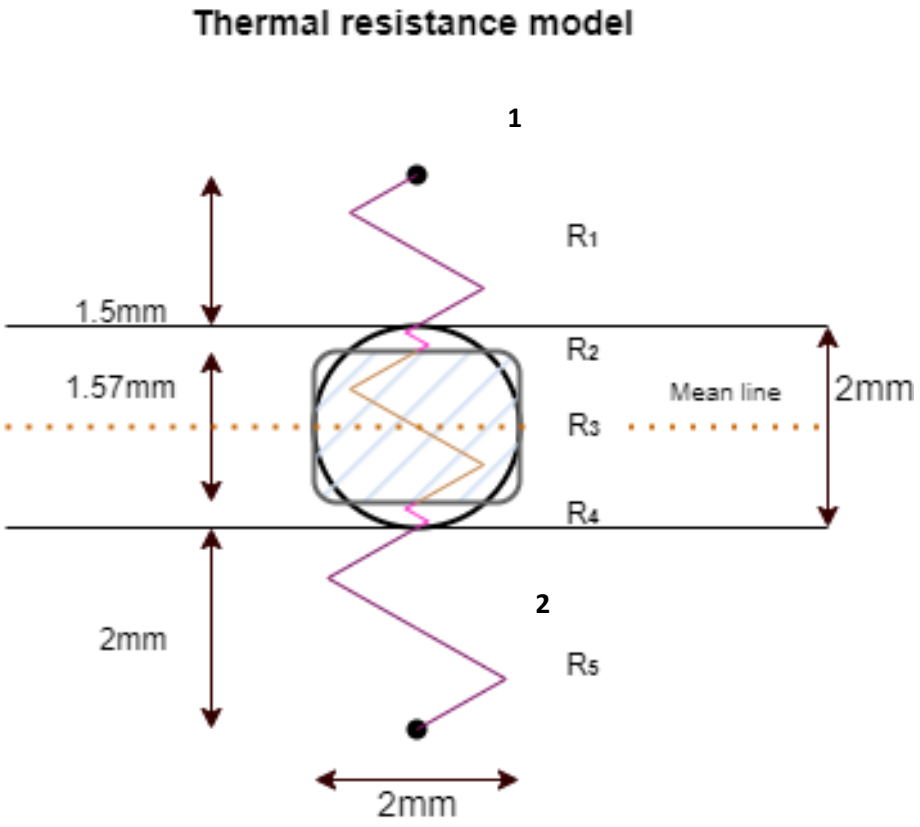

Figure 20 Thermal model for tin sample [2]

There are five resistances in series[Figure 20] which are generated by including the sample between the copper cylinders. $R_1$and R_5 are the resistances offered by the copper material from the location of thermocouple till the contact surface. R_3 is the resistance offered by the tin wire. And, $R_2$and R_4 are thermal resistances of the contact between copper and tin(TCR) which we are interested in and will be used to compare with literature models.

Calculations of these resistances need the accurate temperature profiles of all 5 points in the model but we only have the temperature profile for point 1 and 5 during the experiment. But, by this modelling it deduces the net resistance sources which one might expect while testing, *R'* which is

$$\boldsymbol{R' = \frac{1}{h'} = R_1 + R_2 + R_3 + R_4 + R_5} \quad \textbf{(3.2)}$$

Calculating resistances by using measurements from Figure 19,

$$R_1 = R_5 = \frac{h_1}{k_{cu}} = \frac{1.57mm}{k_{cu}} = 0.00346 * 10^{-3}[\frac{m^2K}{W}] \text{ , } R_3 = \frac{h_3}{k_{sn}} = \frac{1.57mm}{k_{sn}} = 0.0248 * 10^{-3}[\frac{m^2K}{W}] \quad \textbf{(3.3)}$$

Putting equation 3.3 in equation 3.2, $R_2 = R_4 = R_{contact}$, $R_{contact} = \frac{R'}{2} - 0.01586 * 10^{-3}$ which can be written in terms of conductivity as,

$$\boldsymbol{\frac{1}{h_{contact}} = \frac{1}{2h'} - 0.01586 * 10^{-3}.} \quad \textbf{(3.4)}$$

Here the *h'* is the calculate conductivity from point 1 to 2 in Figure20.

Thermal response estimation:

When the experiment is started, all temperatures are noted for regular intervals for around an hour. The temperature T_1 is fitted with the famous exponential curve:

$$T(t) = T_\infty - (T_\infty - T_i) * e^{-\frac{t}{\tau}}$$

Here τ is a characteristic time scale, T_i is the initial temperature (t=0) and T_∞ is the temperature at equilibrium (t=∞). Each variable is adjusted so that its combination produces the fewest residuals in Excel's solver or appears to be the best match. The difference between temperatures is taken using the obtained value and conductivity is equal to $\frac{Q}{A}(\frac{dx}{dT})$. The heat flow (Q) is calculated as the heat released by the flowing water from the bottom, $Q = \mathrm{m}' * C_p * (T_1 - T_4)$. The $\mathrm{m}'[\mathrm{g/s}]$ is the mass flow rate of water which is calculated manually at the start of the experiment, specific heat capacity of water is $4.187[\mathrm{kJ/kgK}]$.

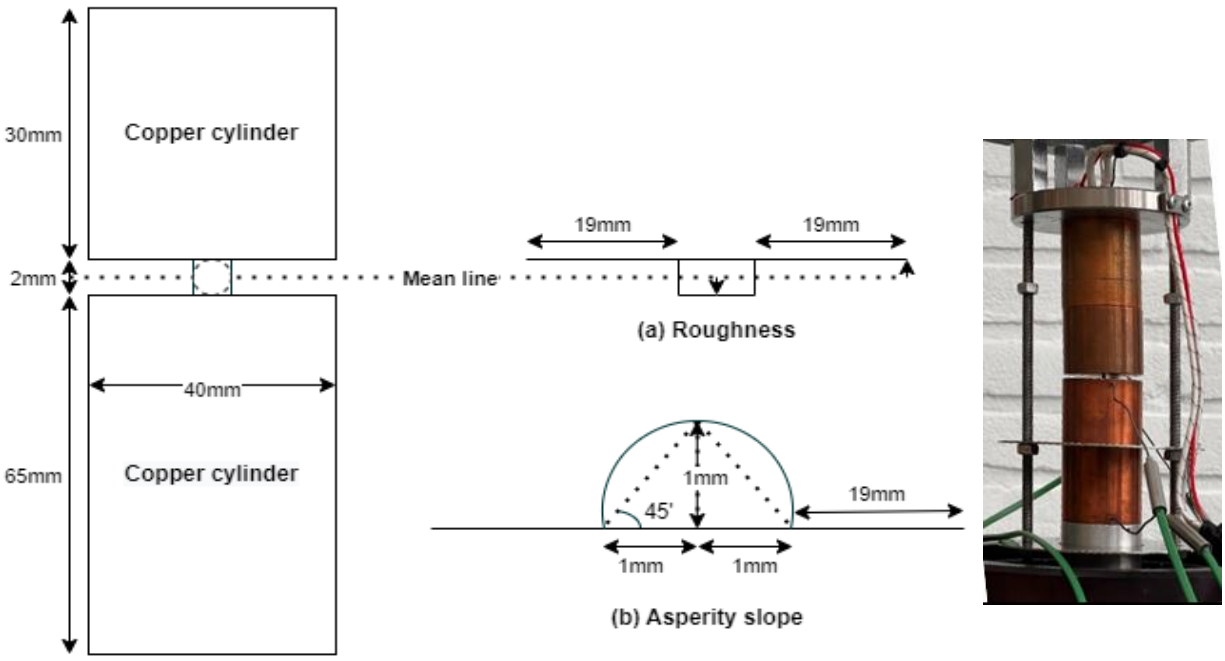

Figure 21(a) Estimation of roughness and asperity with real arrangement

The sample used is 2 mm diameter tin-silver[97/3] alloy wire which is used in soldering. The properties of this sample are young's modulus E = 41.6GPa, thermal conductivity k=63.2W/mK and microhardness i.e. 194.4 MPa[25][26]. The wire is cut into 10 mm length and placed between the copper cylinders.

On the top of the heater, the required load is applied, and heat conductivity is found by the formula $h'=Q/dT*A$ $[\mathrm{W/m^2K}]$. Here heat is calculated with the formula $Q=(Q1+Q2/2)$,

where, $Q_1 = k_{cu}A(T_1 - T_2)/dx_1$,and $Q_2 = k_{cu}A(T_3 - T_4)/x_2$. This Q is used to calculate h'.

For the current test configuration, the actual surfaces in contact are non-conforming, meaning the models investigated in this thesis are not valid. However, in order to still compare test results with modelling results we try to incorporate the non-flatness of the tin surface by modelling a large surface roughness. Although, in this approach we are strictly miss-using the models, for the current investigative scope it will suffice. The roughness is calculated by modelling the wire as a flat surface with contact area as $10\mathrm{mm}^2$.

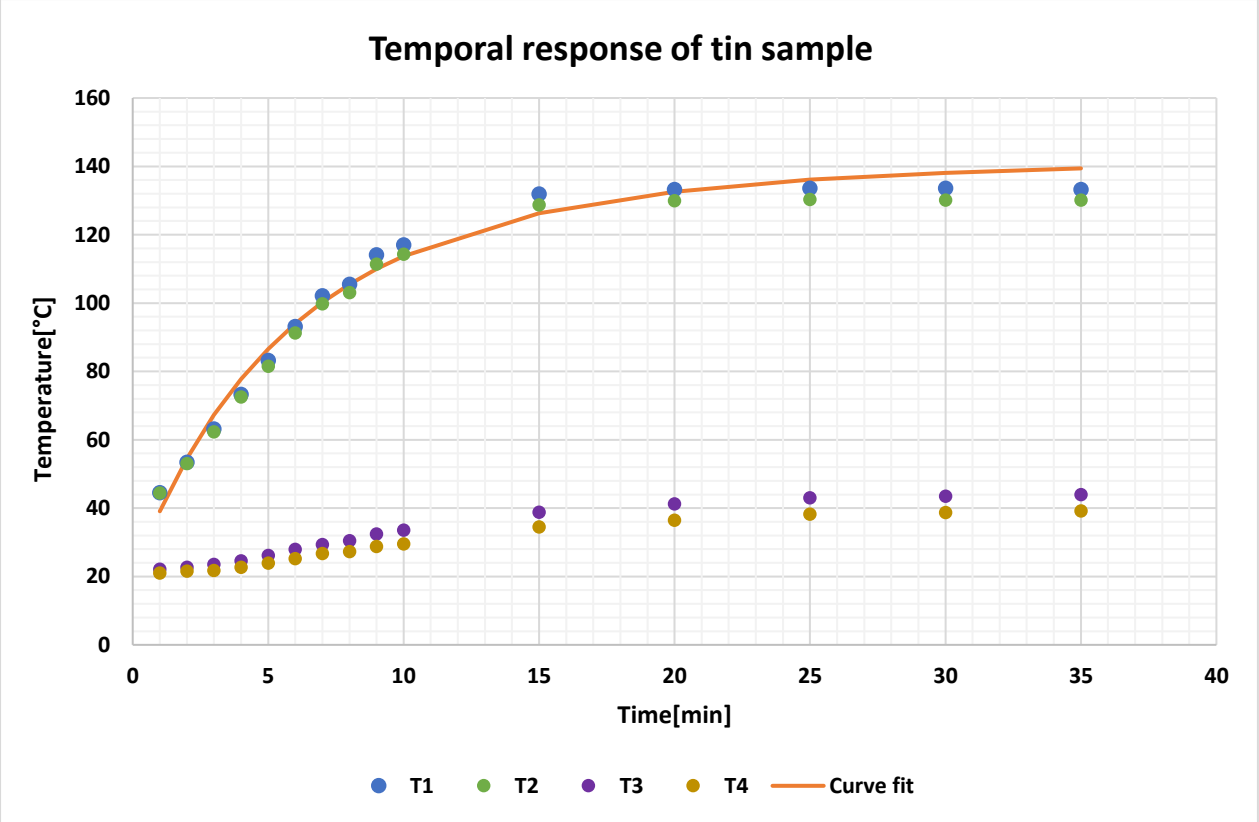

Figure 20(b) Temporal response for tin sample

Figure 21(b) plots all four temperatures for tin wire sample over 35 minutes until the steady state is reached and the final temperatures are noted and used for calculating heat transfer. The curve fit is plotted with the first order fitting equation as mentioned above which is in good order with the first temperature.

Table 2 shows the steady state temperatures for round 3[Figure 22] which are calculated by minimizing the residual in excel. For a sample at room temperature, the average time to reach steady state is around 30 minutes .

Table 2 Steady state final temperatures for round 3

T1	T2	T3	T4
134.9	132.6	38.5	34.9
133.8	131.4	41.1	37.4
132.5	130	42.2	38.5
133.1	130.5	43.3	39.5
132.5	130	43.7	39.3

Appendix C contains the calculations in detail for all the data points for round 3. It also displays how the solver in excel is used to calculate the best curve fit and steady state temperatures.

Figure 21 depicts simplifying the surface for roughness calculation. Ideally, the R_a parameter can be calculated as,

$$R_a = \sqrt{\sum(height\ till\ copper\ cylinder\ from\ mean\ line)^2/(number\ of\ heights)}.$$

The height of the top cylinder is taken as the distance between bottom of the top cylinder and mean line of the tin sample. The squared summation of heights is 40 mm which is taken every 1mm over the sample, thus the roughness is calculated to be $R_a = 1\text{mm}$.

We can also calculate roughness by another formula i.e.

$$R_a = (\sum Area\ above\ and\ below\ mean\ line\ )/(number\ of\ heights)$$

which also gives the same result. For calculation of the mean asperity slope, Figure22 is developed where the wire is taken as a combination of two triangles with a base and height of 1mm each which gives an asperity slope *m=tan*θ that is equal to 1. The flat surfaces have no slope thus there are no asperity slopes. The mean asperity slope is,

$$m' = \sqrt{2/2} = 1.$$

We can calculate the Mikic parameter (discussed in chapter 2) for the tin wire as,

$$\gamma = Hc/(E'm')$$

Here from the material properties and mean asperity slope, we calculate $\gamma = 0.00474$ and referring from section 2.2.1, we know that the deformation lies predominantly in the plastic range and same behaviour is expected while performing the experiments.

Note: The wire is modelled as a flat surface where the roughness is assumed to be same as the height from mean line, 1mm and contact area as 10mm^2. Also, the literature models are only valid on flat surfaces in contact.

Experimental Plan:

The sample was placed between the copper cylinders and the first round of experiments were done by applying contact pressures with step of 0.5MPa until 4MPa. The second round with new sample was performed with 0.25MPa pressure step difference for better resolution. For understanding the elastic effects, both samples' conductivities *h'* are plotted.

Outcomes:

Figure 22, we can clearly see that the heat transfer increases with increasing load. We first observe plastic deformation around 2.775MPa which increased the length by 0.6mm and reduced the diameter by 0.06mm. The deformations and their trends are later analysed[Figure 27]. We can observe that the slopes of *h*' is entirely different before and after 2.425MPa. We can deduce that the first plastic deformation happened at around 2.5MPa and the stress-strain graph for upcoming loads lie on the plastic deformation range respectively.

Figure 23 plots the 2nd set of experimental results which was performed on wider range of pressure points. We can observe that when the first plastic deformation is detected, the heat conductivity keeps on increasing. The arrows show the order of pressures applied. We observe that after the first plastic deformation, even the pressures like 1.5MPa displays higher conductivity then the previous point and this keeps on repeating till the round 4.

Also, the plastic deformation slope is less steep than elastic, as the deformation is permanent. The sample of tin is in the form of wire, which has high ductility. It is not possible to reach the fracture point with this apparatus as it has load application constraints. More the pressure, the more elongation of the wire during compression. Figure 25 depicts the effects of plastic deformation when

loading and how the wire will deform because of high ductility under compressive load. The reason is due to the change in slopes of type of deformation and can be seen in stress-strain curve in Figure 24.

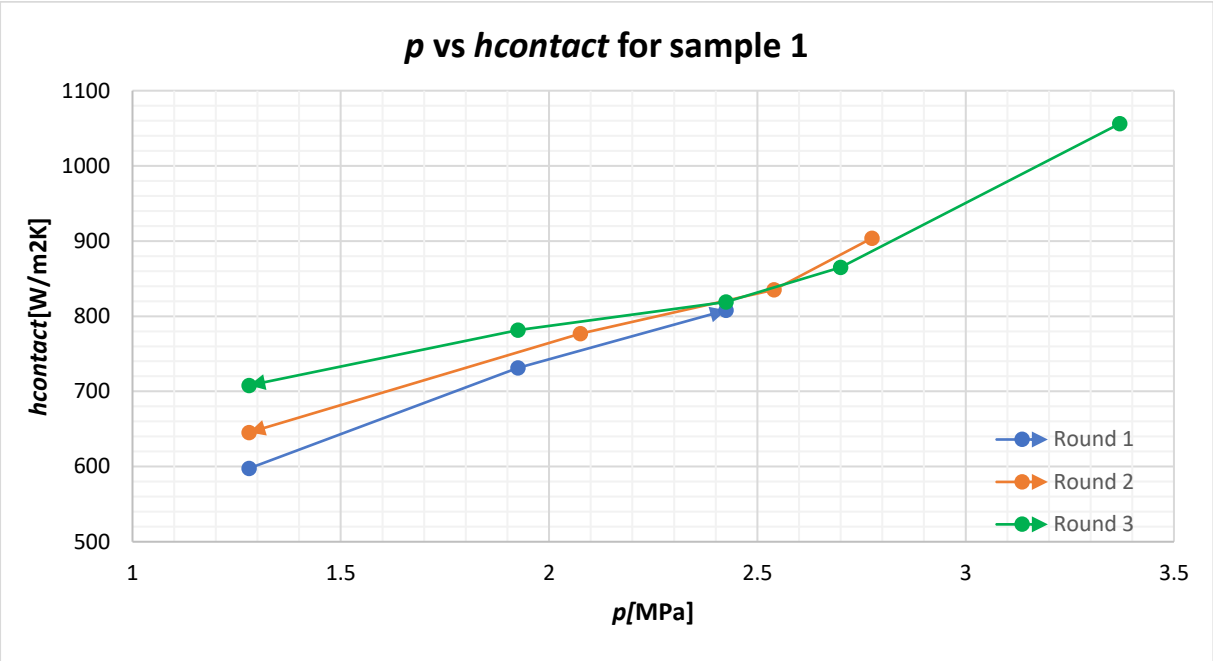

Figure 22 First experiments with tin sample

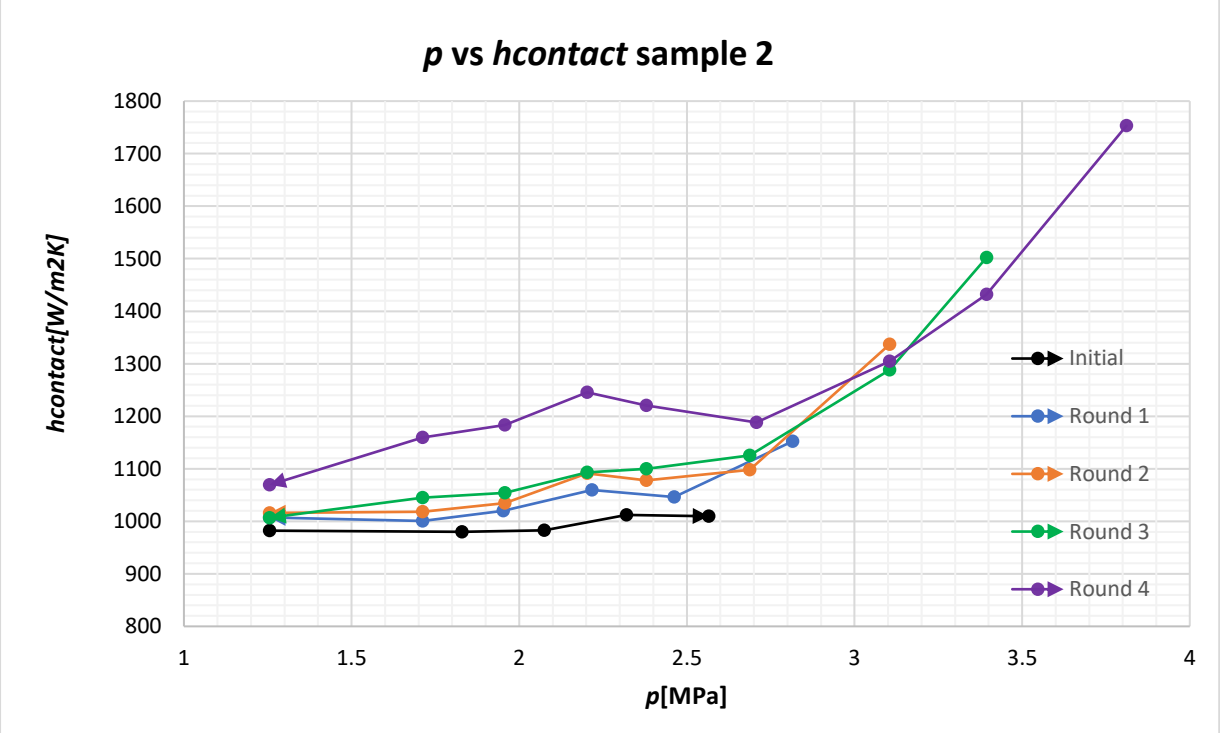

Figure 23 Experiments with second tin sample

For understanding the effect by elastic deformation Figure 26, round 1 consists of experiments with a new sample in the elastic deformation range. Later the same sample is used again to calculate *h'* with same loads. We can observe that the results plotted in both round 1 and 2 lie in approximately the same range and this analysis clears the second part of the hypothesis, that is when the deformation n is in elastic range the heat transfer is same every time under the same pressure.

Hence, the hypothesis we started is true.

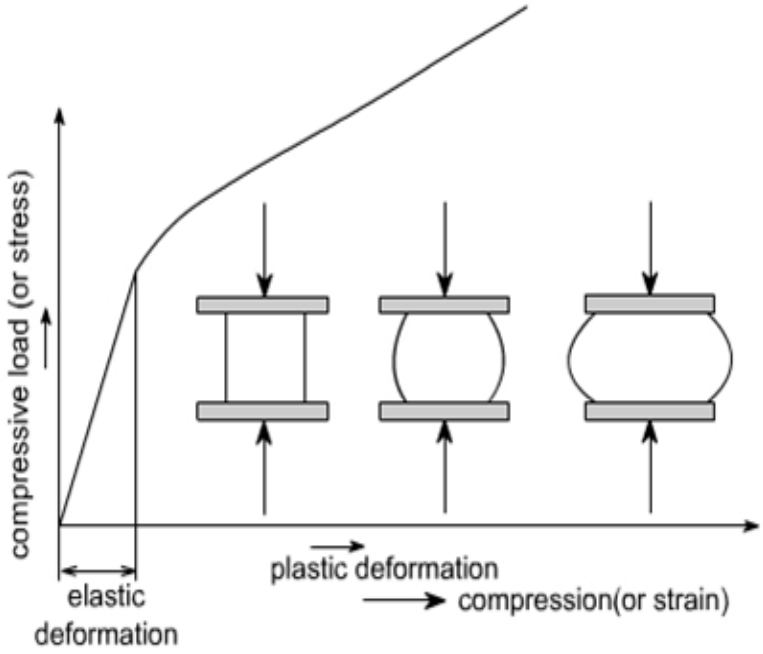

Figure 24 Stress strain curve under compression

Figure 25 Tin sample after and before plastic deformation

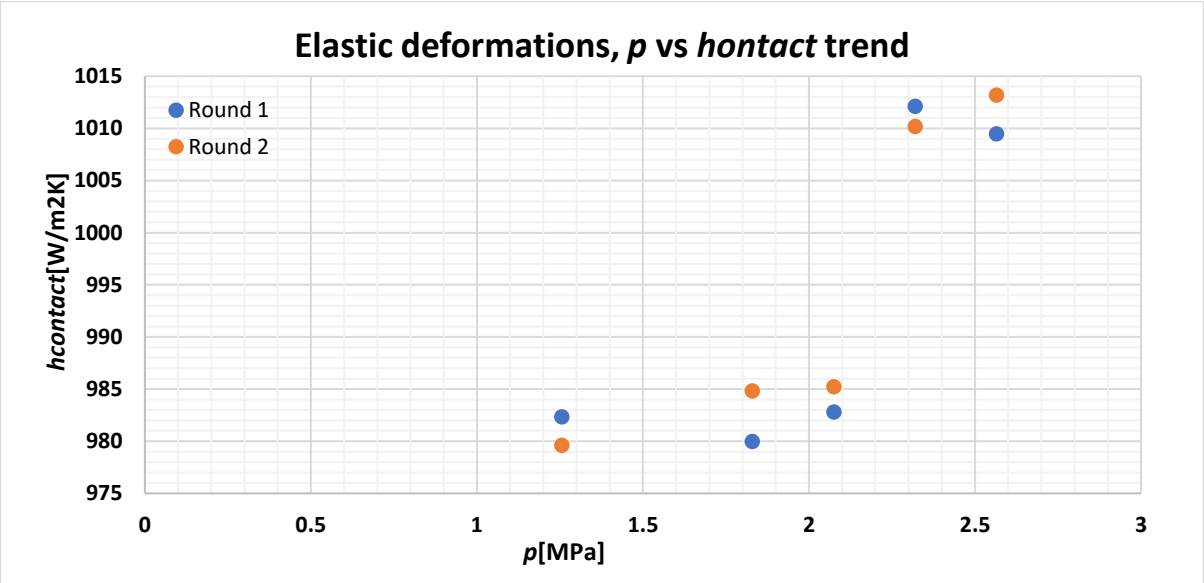

Figure 26 Elastic deformation effect on h'

Additionally, the attempt was made to analyse the plastic deformations among the different contact pressures. Figure 25, we know that there will be no breakage of wire but it will deform. Two deformations were considered:

1. Axial deformation, which is the elongation of sample wire under compression. More the pressure is applied, more will be the elongation of wire.
2. Radial deformation, which is the reduction over radius of the wire's circular cross sectional, as the wire becomes flatter in compression.

Figure 27 plots the deformations along with the applied pressures. We see that for both samples the axial and radial deformations are similar and they completely depends on the applied pressure.

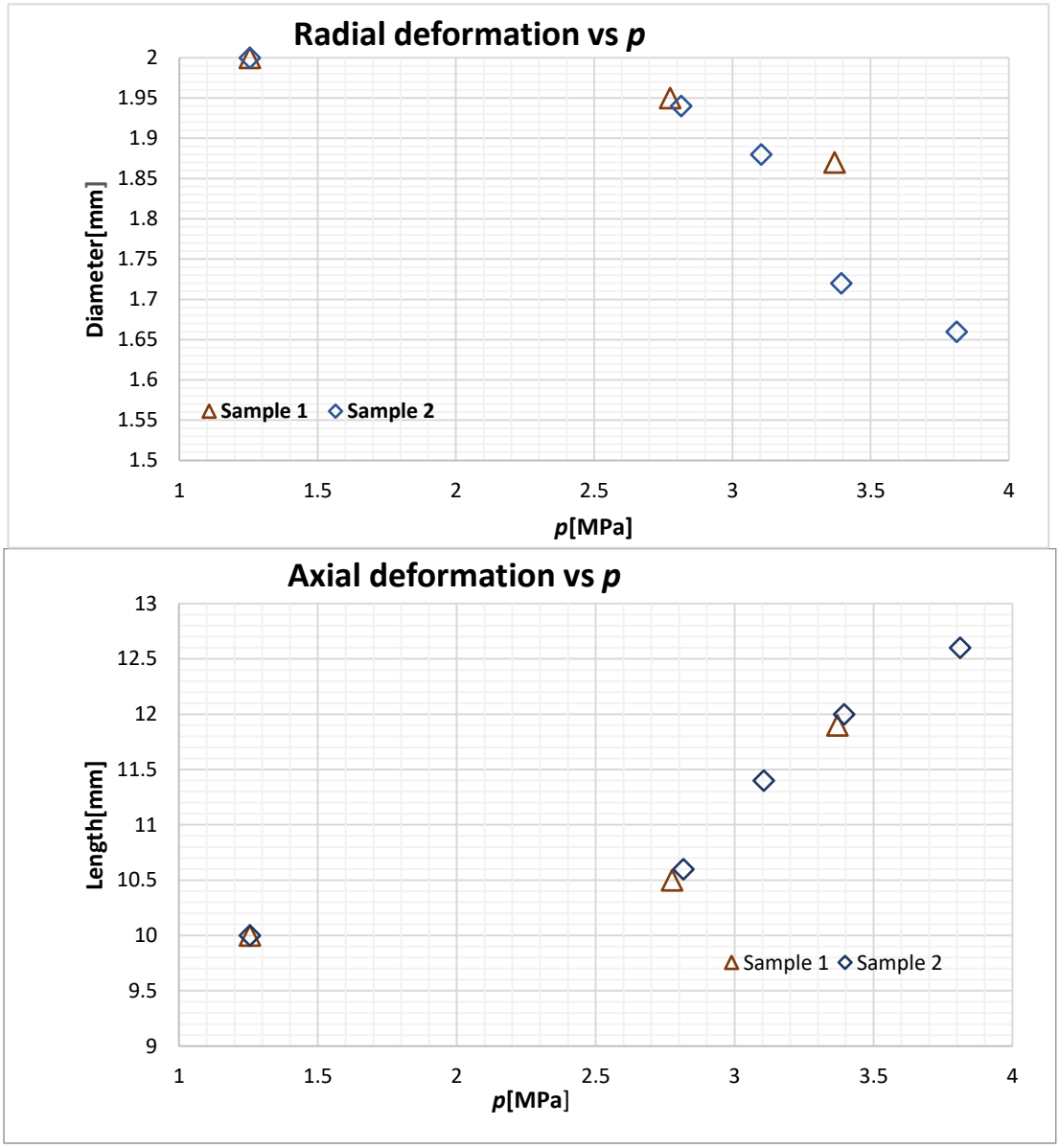

Figure 27 Deformations vs contact pressure

Comparison with literature model:

From Mikic parameter, by initial asperity, we know that the deformation lies in plastic region. While increasing load the asperity slopes will decrease and the Mikic parameter will start to increase due to inverse relation. Thus the prediction of *h'* by Yovanovich and Mikic are plotted along with the experimental results $h_{contact}$ as described in thermal model(equation 3.4).

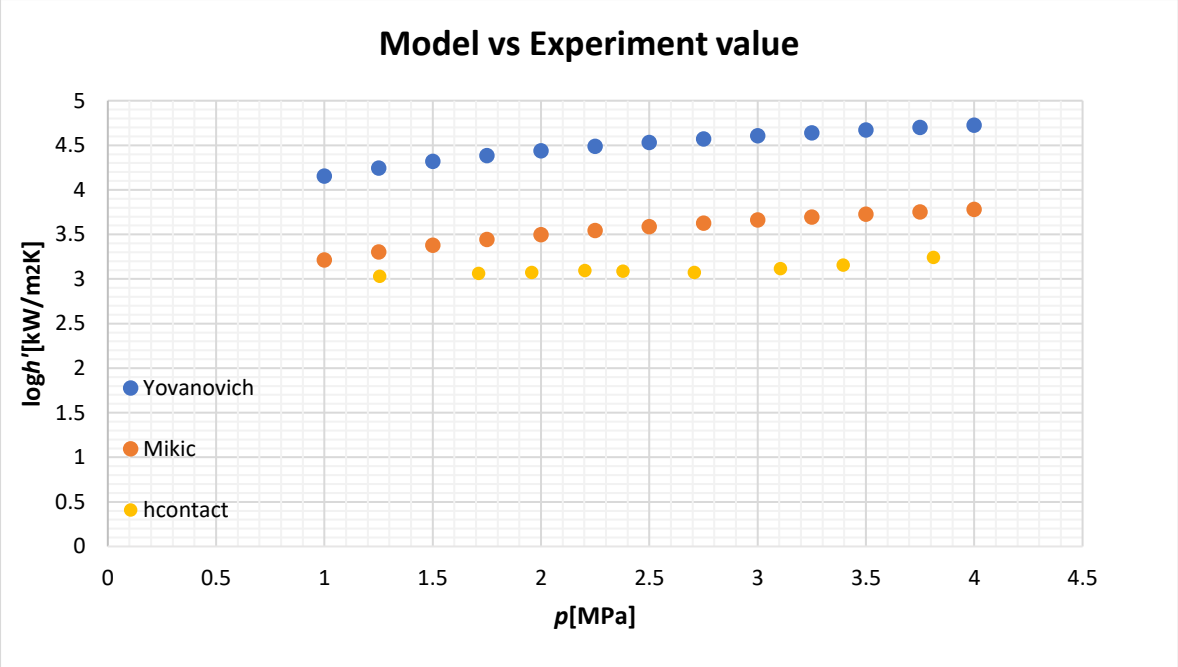

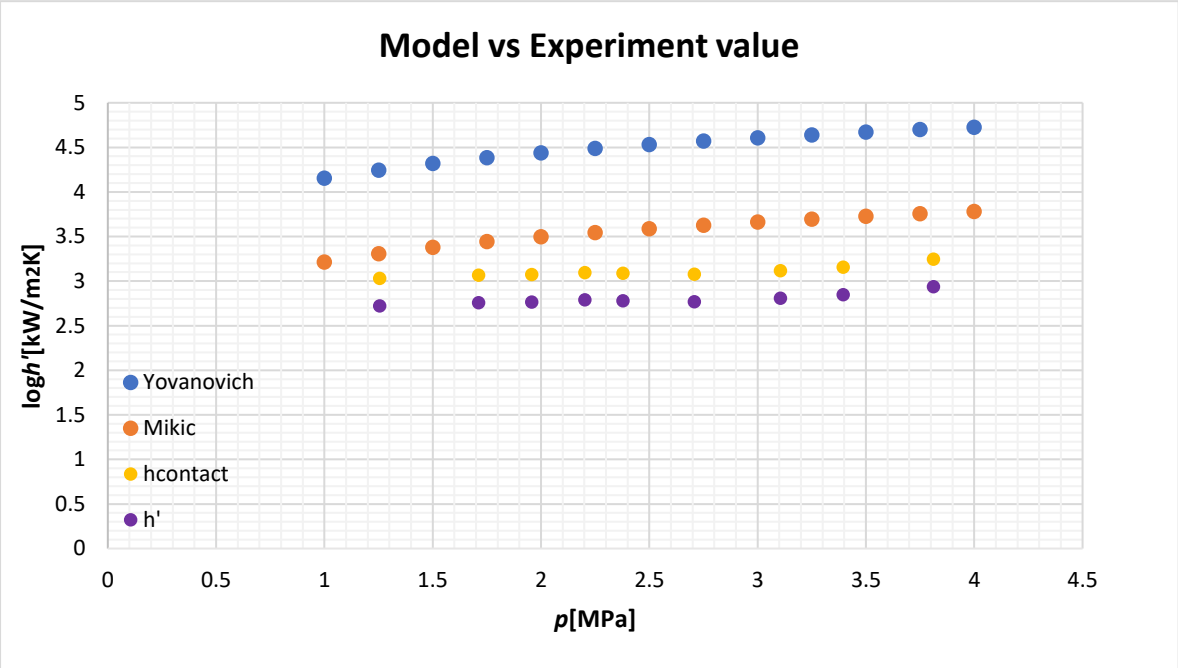

Figure 28 Model prediction vs experimental values

Figure 28 plots the experimental data of 1st sample and the respective calculations of Mikic[2.10] and Yovanovich[2.13]. As we can observe that the predictions of the yovanovich model is somehow around 10 times of the actual calculated value, which is in different range. We still see that Mikic model is closer to predict the experimental which is still around 3 times more.

This difference in prediction can be due to change in real contact surface area as discussed in chapter 2. Due to lack of research in this domain, there is a need to research and verify their general applicability.

More detailed plots for *h'* are plotted in Appendix C, which also compares the $h_{contact}$ with the total conductance from point 1 to 2 in thermal resistance model which includes all 5 resistances on a non-log scale [Figure 20].

The next chapter will help to understand the *h'* dependence on pressure with a different experimental setup.

4 Experimental Methodology(ii)

For a detailed understanding, another test setup in Philips Engineering Solutions[PES] is used to perform experiments. First, the major components of the test setup are discussed. Later, the layout of the experimental setup is explained with its working. Furthermore, the outcomes and its correlations with theoretical models is addressed.

Components:

- **Heater power source**: The electrical power input is used for the heater.
- **Heater plate**: The plate is made of aluminum and placed above the samples. Sample 1 transmits the heat.
- **F-stop pin and bolt**: It helps to measure the applied pressure(*p*) by tightening a screw.
- **Multimeter**: Two multimeters are used to measure current, voltage and force applied via screw.
- **Vacuum pump and chamber**: Used for creating a vacuum environment for testing.
- **Pressure sensor:** Pressure sensors are used to display applied contact pressure.
- **Water cooler**: The water is circulated at the setup's bottom to maintain temperature during the readings.
- **Temperature sensors(NTCs)**: Thermistors are placed in different locations to understand the behavior of change in temperature and calculate heat transfer coefficient(*h'*). NTCs are used to measure temperatures every 5 seconds and plot the readings on the computer.
- **NTC readout instrument**: An agilent data acquisition system is used to measure readings from thermistors for the entire experimenting time and logged-in computer.
- **Radiation shield**: Aluminum shield around samples is used to reduce radiation losses.
- **Elevation block**: A large block beneath the cooling plate is used to adjust height of the frame.

Figure 29 Test Samples

- **Test samples**: The samples are in the shape of a cone with a flat peak having a contact area of 50mm^2. They are available in different materials i.e. alloys of aluminum, titanium, and steel.[Figure 29]

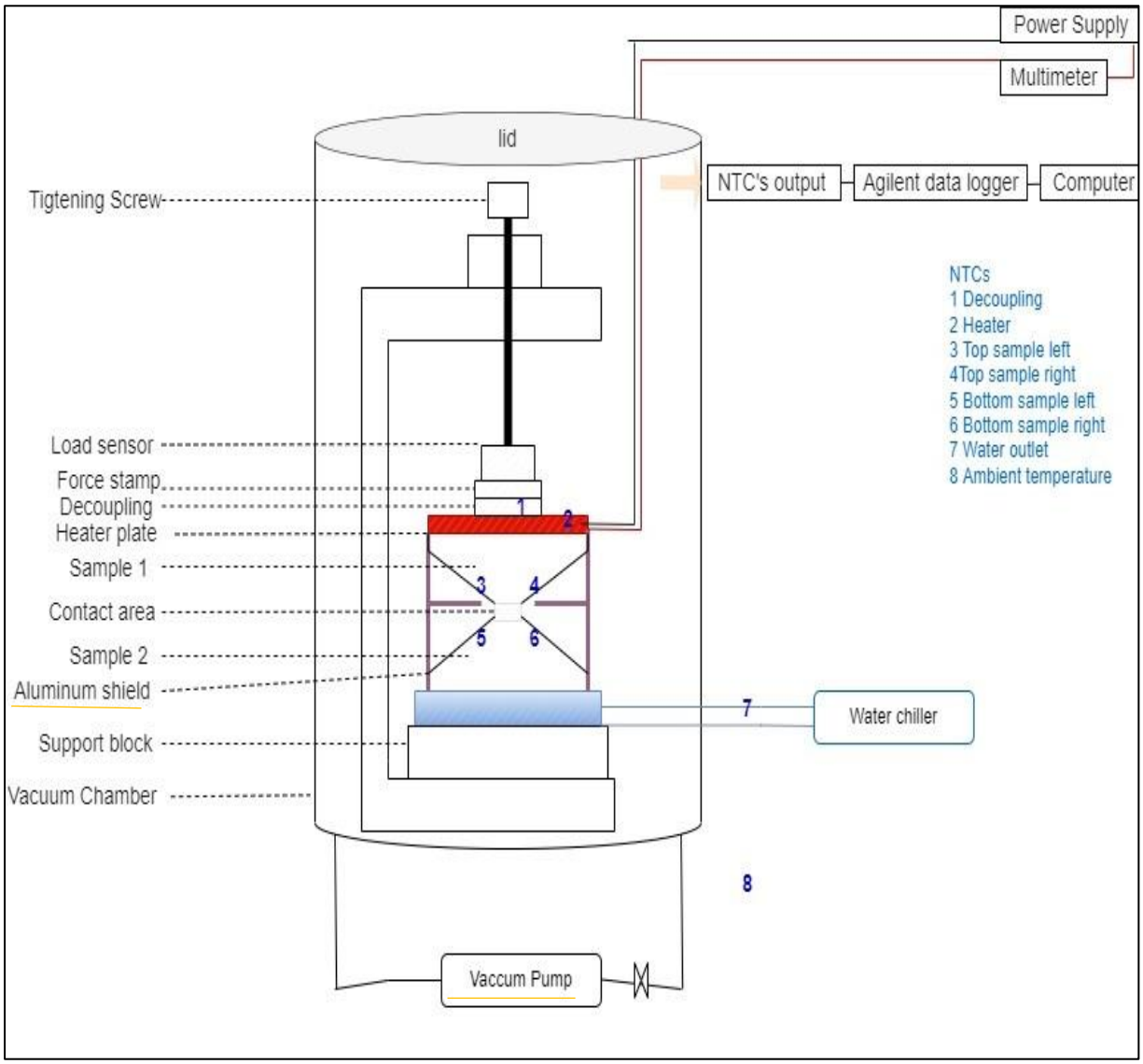

Figure 30 PES test setup layout

4.1 Working of the experimental setup

The samples are in the shape of a cone with a circular flat top of an area of $50mm^2$. They are cleaned with Isopropyl(IPA), to remove dirt, and assembled on the support block. The heater plate is on top of sample 1, and the aluminium shield is placed around the samples. The pressure applied is measured by the load sensor. An Allen key is used to screw the bolt until the desired pressure is obtained and is then checked by a multi meter display. Then the setup is gently placed inside the vacuum chamber.

The NTCs are connected to and logged via a data acquisition system. There are 8 NTCs[Figure 25], two on each sample, to find the net temperature difference from the contact area(3,4,5 and 6). The heater temperature is measured by the 2nd NTC, and the decoupling temperature is measured by the 1st NTC. The other two thermistors are for ambient air and water temperature after leaving the cooling plate(7 and 8).

After successful connections, we connect the water couplings to the bottom pipes and start the water chiller. Once the water flow is constant, the vacuum chamber is closed by placing lid on top. The lid is tightened by placing four screws equidistantly for proper support. Next, the vacuum pump is started. The screws must be tightened along with the running pump to vacuum more quicker. Once the pressure reduces to a few Pascals(<9Pa), the heater is started and temperatures are recorded every 5 seconds till the steady state is reached. Then, a more refined result is obtained by curve fitting the data with similar approach as in chapter 3.

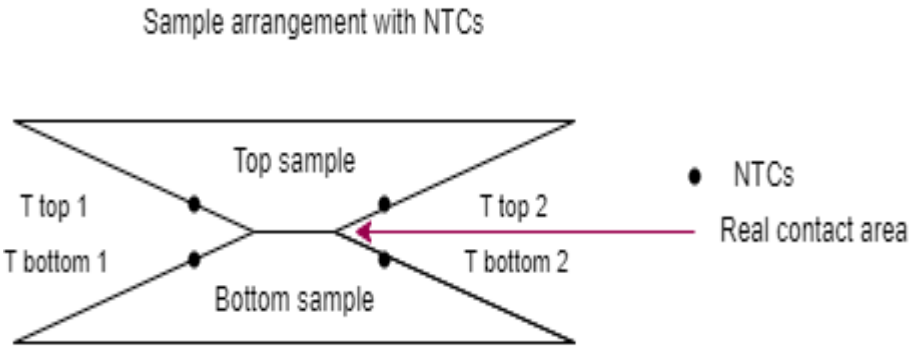

Figure 31 NTCs location on sample

Figure 31 displays different location of NTCs on the bottom and top samples, which are labelled as the T top 1,2 and T bottom 1,2. They are plotted and fitted by the relation stated in the *h'* calculation(Eq. 3.4). Their average is taken to calculate T_{top} and T_{bottom} which is used to determine the dT with the compensation factor β to determine *h'*.

Figure 32 displays a typical trend of the temperatures, an example of the plot for steady state and curve fitting. The graph is temperature vs time, and it plots 7 NTCs. The reference NTC is installed over the heater and decoupling is the atmospheric temperature near setup.

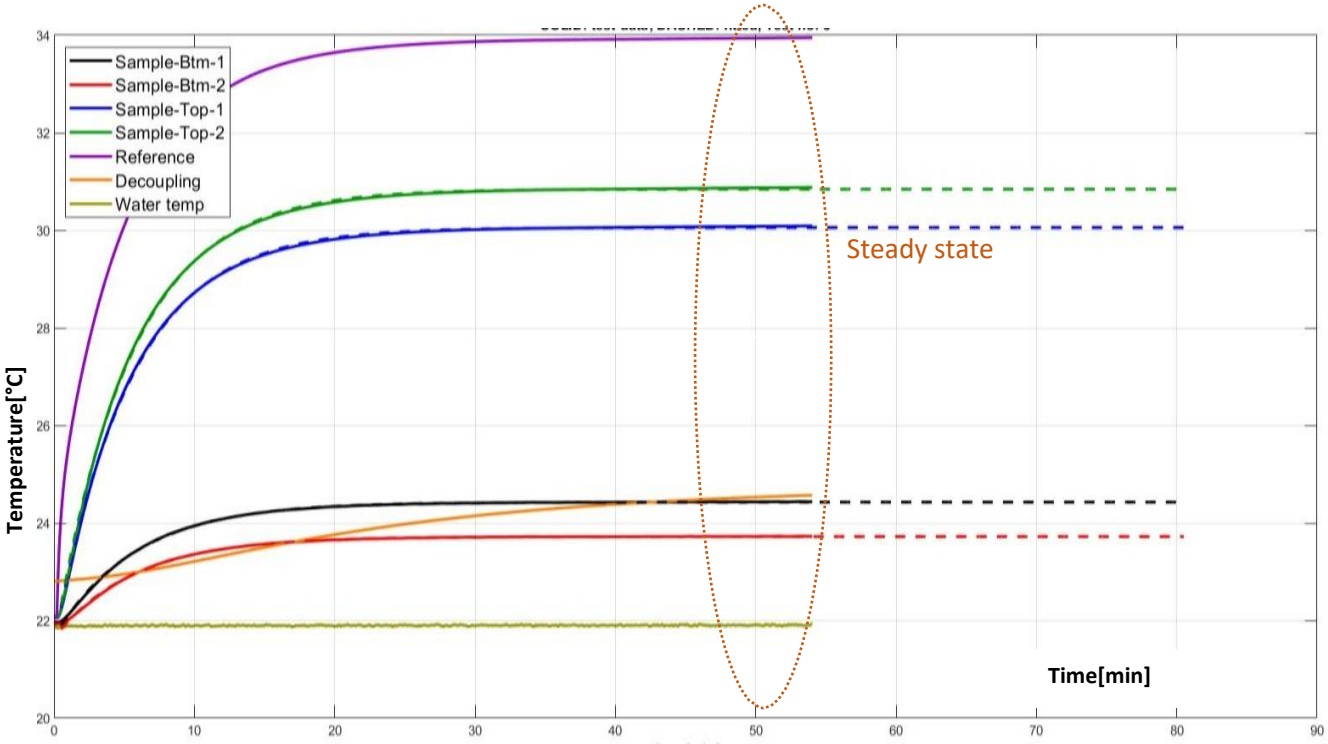

Figure 32 Temp vs time graph for AL5 (Ra=0.4 µm) for 0.5 MPa contact pressure. Curve fitting and steady state temperature identification.

After all the temperatures are approximately constant, steady state is reached which is denoted by the dashed area in orange colour.

h' calculation:

The *h'* calculation is done by a MATLAB code. Where 8 NTCs measure the temperatures and input to data acquisition system that is connected to the MATLAB code. The code plots all temperatures as shown in Figure27.

The temperatures are fitted with relation similar to chapter 3, that is $T = y + y'e^{\frac{-t_{fit}}{\tau}}$. Where t_{fit} is the vector used to calculate the range of fit, taken as 80 minutes. Variable τ is the time taken to reach steady state. y and y' are the initial and instantaneous time recorded.

The NTCs are not exactly on the contact surface as seen in Figure26, thus there are fitting parameters taken for top and bottom sample, named as β. β is the thermal resistance between NTC measurement location and actual contact interference of top and bottom sample. It is taken as 0.19 [K/W] for this sample setup. This is used in calculations for *h' as,*

$$dT_{corrected} = T_{top} - T_{bottom} - Q(\beta_{top} + \beta_{bottom})$$

as both top and bottom correction factors are same, the equation is,

$$dT_{corrected} = T_{top} - T_{bottom} - 2Q(\beta).$$

h' is calculated with heat equation formula

$$h' = Q/(A * dT_{corrected})$$

Limitations of the setup:

- While stacking the samples, the problem of alignment and orientation arises, it can affect the results and depends on who is the operator and the number of times it is removed and installed.
- The water couplings are fragile, and there are chances for them to fail in the long run. Similarly, the NTCs might fail during the experiments and invalidate the readings.
- For applying pressures above 25MPa, the sample area needs to be reduced, which leads to non-reproducibility. Thus, the results are inconsistent with the previous study [14].
- The power for the test campaign is taken as 1 watt. However, a previous study[14] shows that *h*' is constant for different heat flux.

4.2 Correlation of Experimental data and literature models

This section explains correlation between the models and experimental results. It also deals with the development of an empirical relation of different roughness. Section 4.2.1 discusses the outcomes of experiments with different trends of the h' with different factors. Later in section 4.2.2, the literature models are compared, empirical relations are developed, and the reproducibility is checked. At the end of the thesis, some experiments were performed, continuing with the previous samples of Aluminum 5083. After around 30 days, experiments are performed, which aim to understand the reproducibility over timeThis has already been referred in literature study(2.3.1) where Baharami[10]

coated his aluminium samples with tin as aluminum tends to react with oxygen in the air and form a oxide layer which might affect the *h'*. Also, another set for understanding the rotation/alignment effects on *h'* is performed in section 4.3.

4.2.1 Outcomes of the Experimental campaign

1. Roughness R_a=0.4µm (Recontacts and reproducibility)

The aluminum sample(Al5083) experiment (sample numbers 5 and 6 with roughness parameter R_a=0.4µm) is done according to the experimental plan and plotted with the results as reported in [14].

Figure28 plots the experimental results which are compared with the data of previous tests[14] named 'PINs'. The Experiment and recontacts are in good agreement with the previous experiments done by PINs. The orientation and alignment of the test samples were kept constant, and the samples were not disturbed and were not cleaned after each successful test. Hence, the reproducibility is good in these conditions.

There might be relative deviations when the alignment changes, but the setup seems reproducible under undisturbed orientation. The relative uncertainty range seems constant for the constant pressure range, that is around 10%. The samples have been used 15-20 times earlier. Therefore, an empirical relation can be made for these particular set of samples providing the setup itself is reproducible for pressure range 0-25MPa.

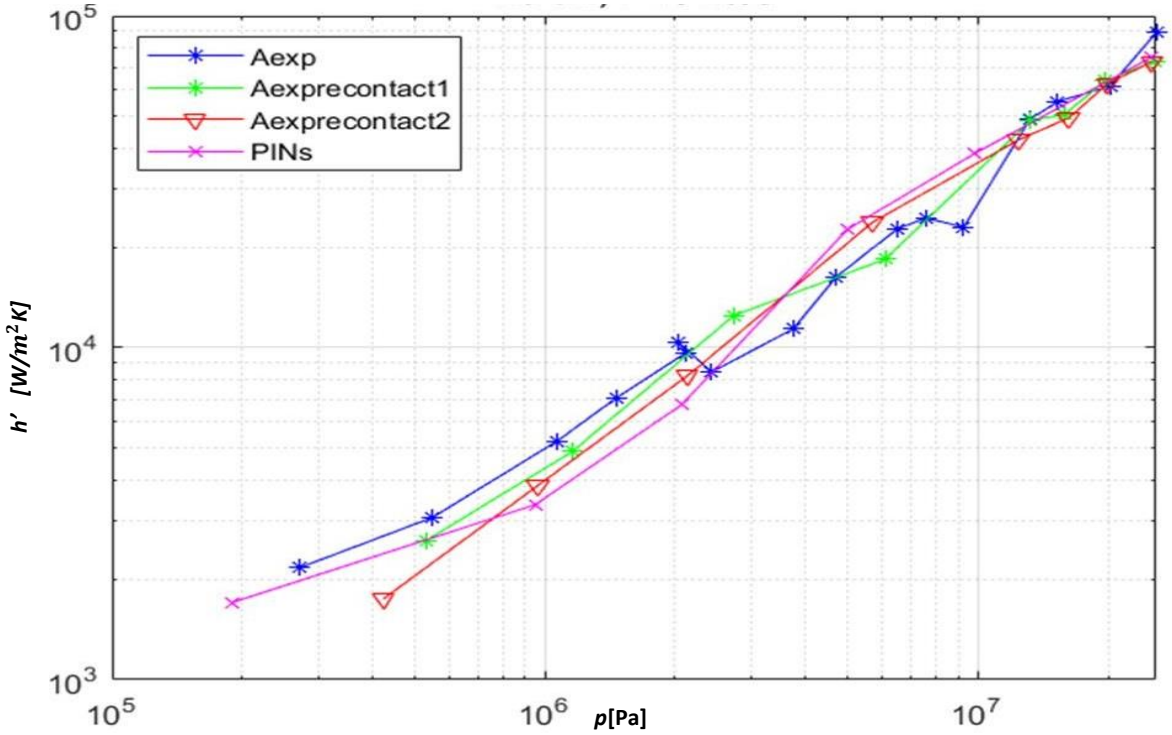

Figure 33 comparison for Al5 (5-6)

2. Roughness R_a=3.2µm (Reproducibility)

Next tests were performed on a set of samples of 3.2µm roughness and compared to the previous readings for the same roughness value[14]. Figure 34 plots experimental results with previous tests denoted by 'PINexp'.

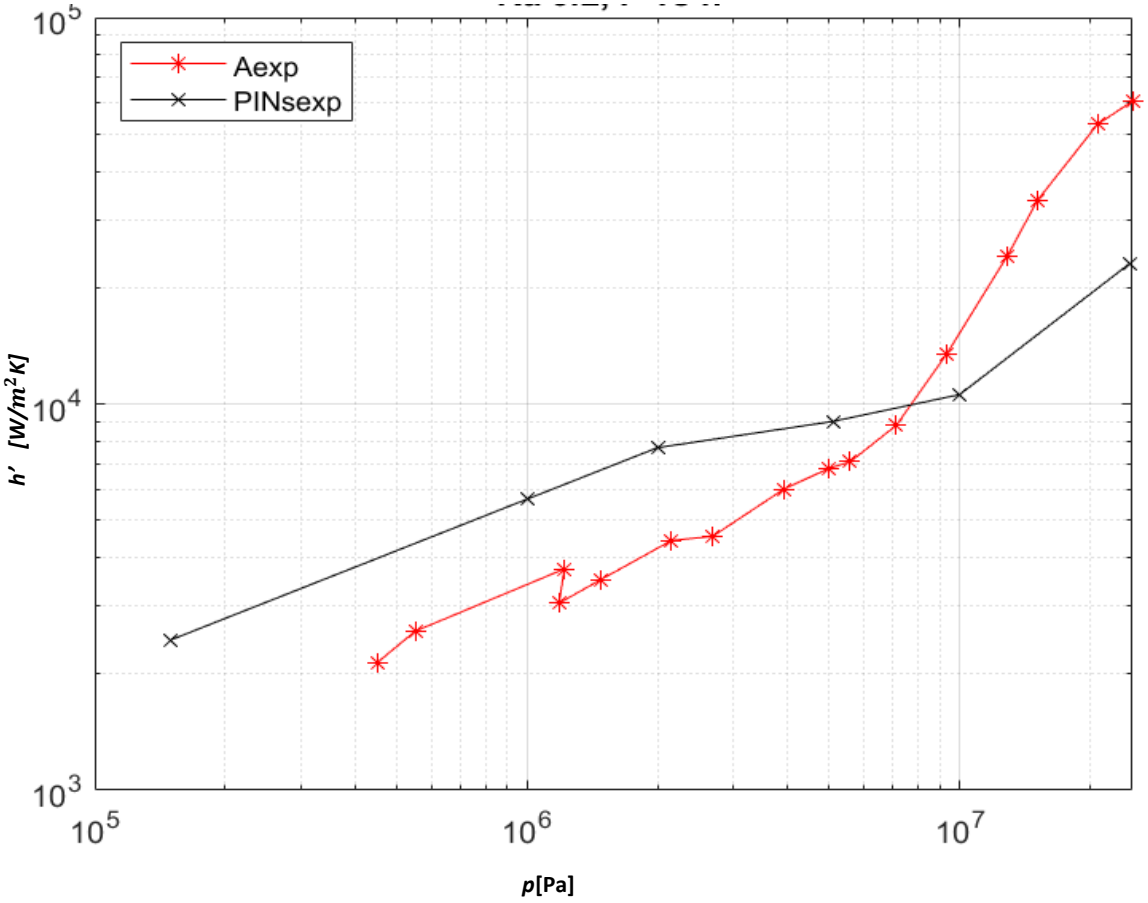

Figure 34 Comparison for Al5083 (45-46)

It can be observed that there is little correlation between the current and the old experiments, as the h' trend in both the plots are entirely different. However, the samples were again, same for both plots, and the number of experiments in the PINs report is low to be conclusive. There is only one data point at a pressure beyond 10MPa. Therefore, there is a need for more data points for deriving conclusions. It can be observed that there is a change in slope at around 7MPa.

3. Roughness R_a=0.4µm and R_a=3.2µm (Roughness effect)

Figure 35 plots experiments of the combined data points of all roughness. Some speculation can be made to understand the physical reason behind the behaviour of the *h'* with contact pressure by altering the roughness value. There are not many data points available for higher roughness, but it is visible from the plot that increasing the roughness value decreases the *h'* value which is expected as discussed before in chapter 2. It is because a rougher surface has sharper asperity slopes which provides less contact between two surfaces which affects conduction

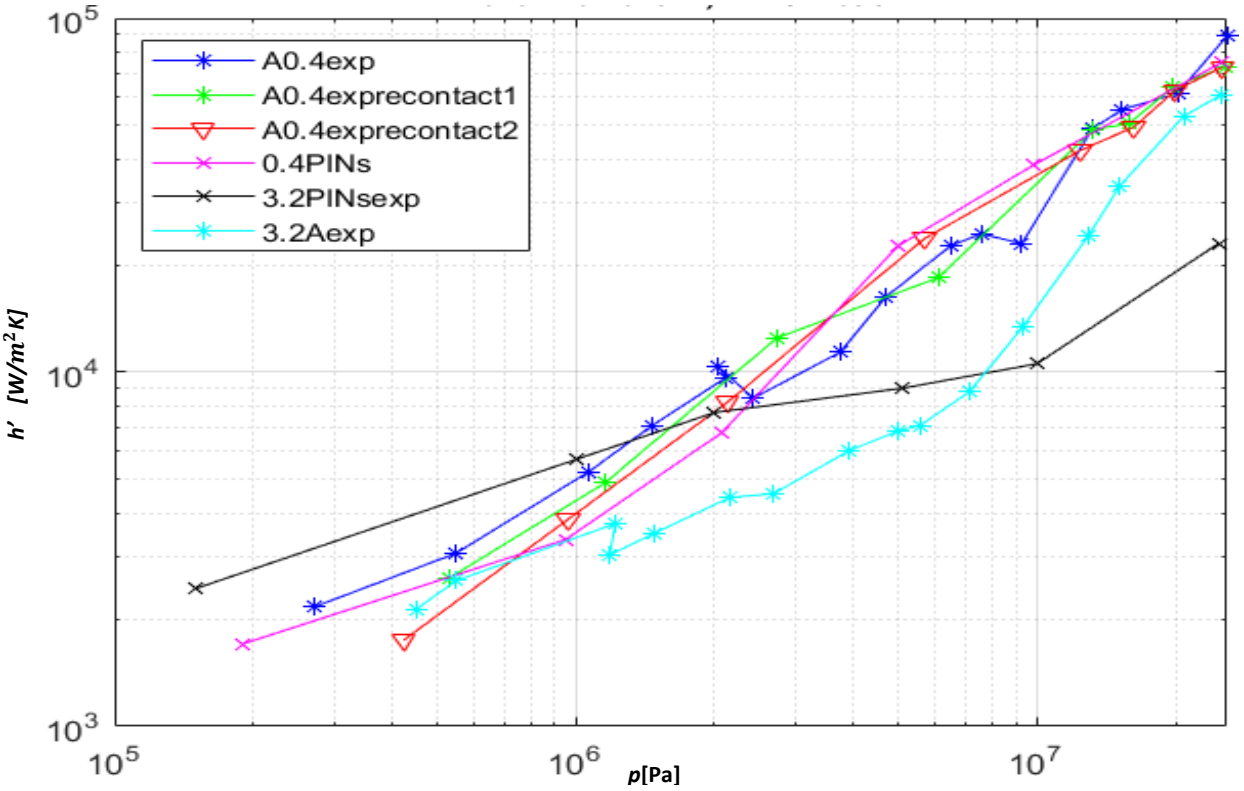

Figure 35 Roughness-h' comparison

4.2.2 Correlation with literature models.

After the curve, empirical relation can be developed for R_a=0.4µm as the tests are found to be reproducible. From data analysis we found that the *h'* is directly proportional to the pressure to a power 'a'. With this idea, a curve fits with the relation $h' = Ap^B$ is done. Here *A* and *B* are constants. The curve fitting is performed in MATLAB with the least square error method function 'lsqcurvefit', where the selected range is plotted for A and Figure36(a) plots the curve fit. Figure36(b) represents the mesh plot for constants A and B, along with the root mean square of errors of the data points on the z-axis. To find the minimum of the combination of A and B, Figure36(b) represents that the minimum lies in a dark blue area. The *B* value is 0.876, which is in the same range as the literature model equations. *A* is found to be around 4.5.

The relation obtained by this curve fit is *h'* =4.5190$(p)^{0.8760.}$

These are compared to equations of Mikic(2.10) and Yovanovich(2.13) as discussed in chapter 2.

Literature models correlation and empirical relation for Al5083 and R_a=0.4µm:

The constant *B*, which is 0.8760 is in comparable range to the models of Yovanovich(2.13) and Mikic(2.10), which have 0.94 and 0.95 as their exponents of pressure. By understanding physical relations, the constant *A* can possibly compress some factors. For example,

- '*A*' Consists of an effective thermal conductivity of the samples

Here Al5083 has *k* as 117[W/mK], and effective thermal conductivity is calculated as, $k = k_1k_2/(k_1 + k_2)$. For this case, k_1=k_2=*k*, then *k=k/2*, which is 58.5W/mK

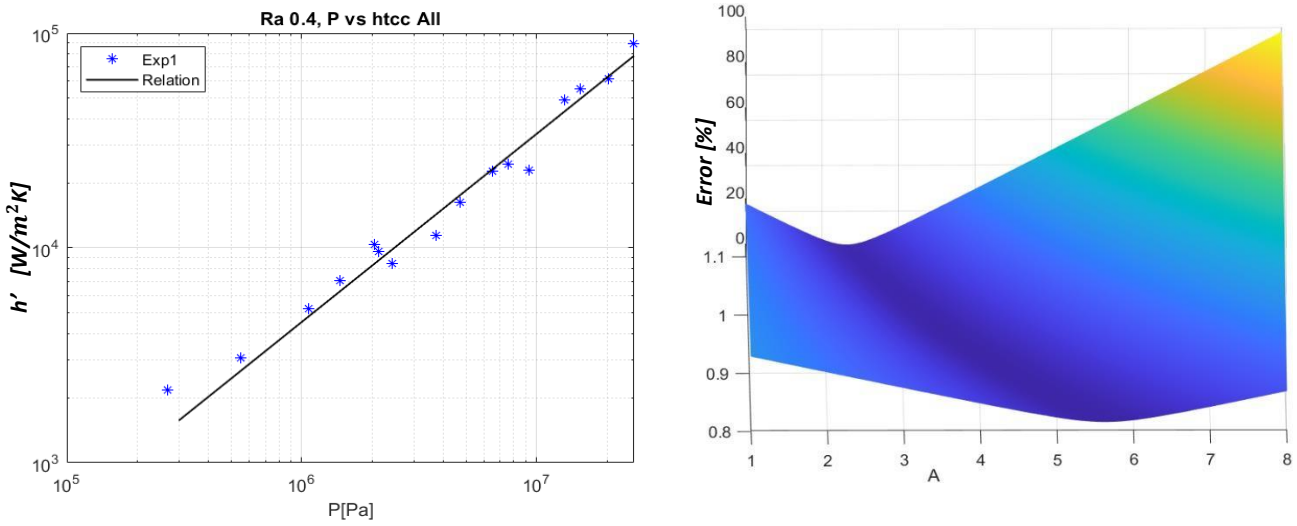

Figure 36 Fitting curve relation for Al5083 Ra 0.4 µm

(a) Fitting Relation for Ra 0.4µm *(b) A and B minima plot*

- Effective R_a parameter(0.566µm)

Here the surface roughness parameter is R_a =0.4µm. As two surfaces are in contact, both effects will be R_a 's root mean square value.

$$R_{a'} = \sqrt{(R_{a1}^2 + R_{a2}^2)}$$

Here $R_a = R_{a1} = R_{a2}$, Thus $R_{a'}$=0.566 µm

- Real contact area(F_k)

When the surfaces are entirely smooth, the roughness decreases. It thus increases the actual area in contact due to lower asperity slopes. Thus, to balance, a dimensionless parameter is taken,

F_k =Percentage of Actual area in contact. Also, this factor may change while changing pressure, as pressure might deform the surface plastically and increase the actual contact area.

Finally, A can be written as $A = k * F_k / R'_a$ [103.44Fk].For the developed relation, we have *A*=4.5190. The unit of *h'* here is kW/Km^2. *A* consists of all the possible contributing factors which are used in the prediction of *h'*.

Yovanovich $h' = 4.2 * k\left(R_{a'}^{-0.257}\right)\left(\frac{p}{H_c}\right)^{0.95}$

Mikic $h' = 2.83 * (10^{-3}) * k\left(R_{a'}^{-0.955}\right)\left(\frac{p}{E'}\right)^{0.94}$

FVV $h' = 0.008\frac{k}{R_z}(\frac{p}{H_b}U(H_b))\text{^}10\sqrt{\left(\frac{p_o}{p}\right)}$

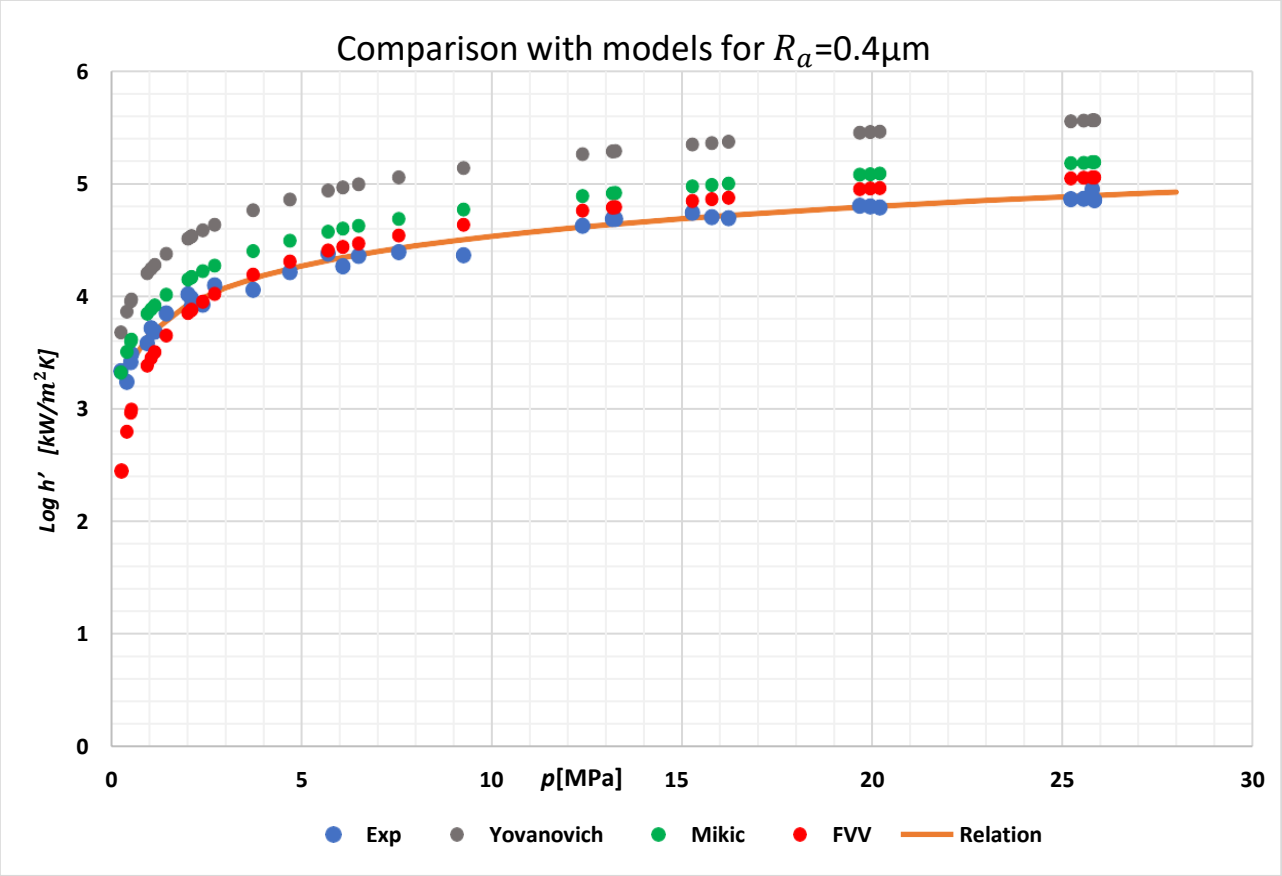

Figure 37 Comparison with models and developed relation

To make the relation comparable with the equations, hardness is introduce in calculation in the final equation developed is $h' = A'\left(\frac{p}{H_c}\right)^B$ The final relation remains unchanged but is more comparable for calculation.

Developed relation $h' = 1640.67\left(\frac{p}{H_c}\right)^{0.8760}$

Yovanovich $h' = 10831.18\left(\frac{p}{H_c}\right)^{0.95}$

Mikic $h' = 213292\left(\frac{p}{E'}\right)^{0.94}$

FVV $h' = 1744.966(0.0057p)\text{^}10\sqrt{(\frac{p_o}{p})}$

Figure 37 displays semi log plot of *h'* and data with different models and developed relation predictions. All the models exceed the measured value of *h'*, which is expected as other models consider absolute conditions. Out of all the models, FVV seems to fit better. The deviation in prediction by FVV can be because it considers one atmospheric pressure.

The prediction by the developed relation is in good order with the experimental data, but it certainly has some constraints such as the non-reproducibility of the found *h'* upon changing the conditions that is cleaning the surfaces or changing orientation.

Also, the relationship needs to be checked before using.

Limits and constraints:

- The developed relation is valid for specific material properties and surface parameter. For checking validity on other materials more experiments should be done.
- The relation is developed for experiments done in the pressure range till 25Mpa.

Thus, it can be inferred that the application scope of the formula is limited. Also, developing a generalized model is complex.

Reproducibility:

The relation is plotted with the experiments done in PES by Marcel Kawalec, who is currently pursuing his thesis in Philips on the same setup. Figure 38 depicts the developed relation prediction to previous experimental data set. The test setup results are reproducible and in good order with the developed relation. Thus, the developed relation is adequate for the prediction of h' for Al5083 material (Ra=0.4µm) for the experiments performed on the Philips test setup with a pressure range of 0-25 MPa. The reproducibility was not observed in the Philips experiments done in 2019[Section 2.2 [14]]. This might be due to the formation of oxide as samples were tested after a year.

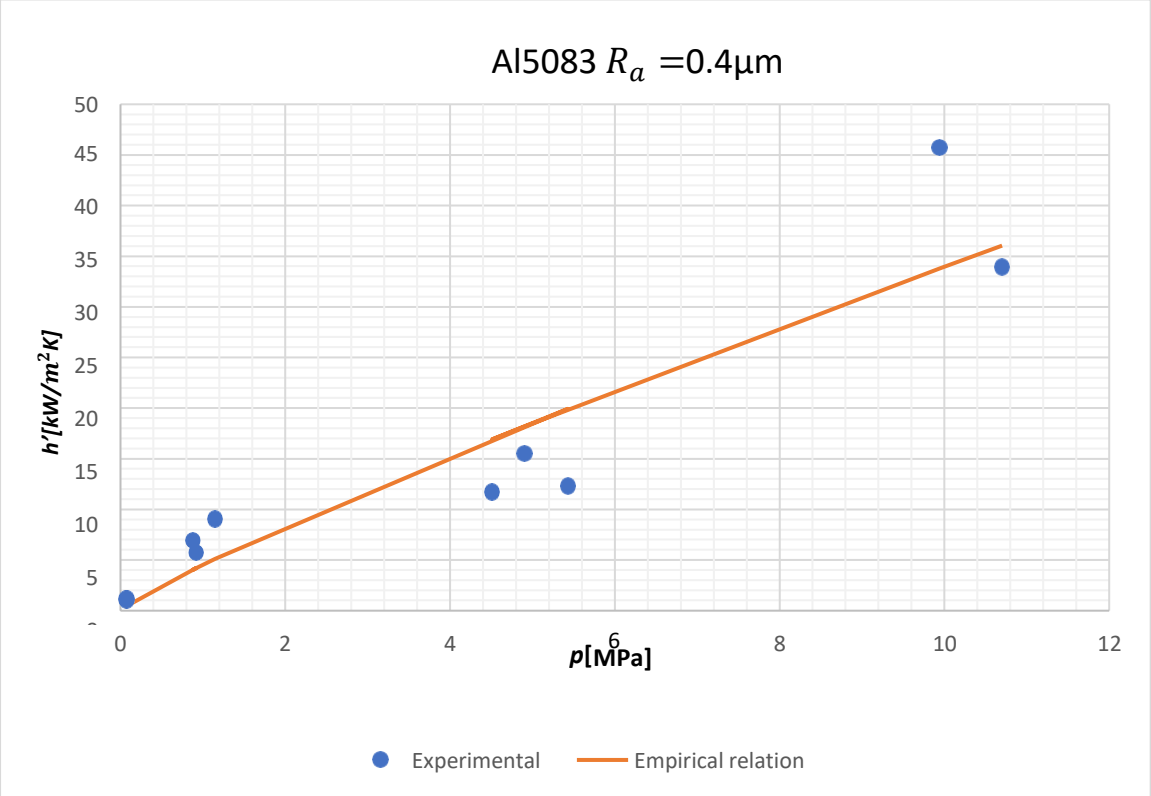

Figure 38 Setup reproducibility

4.2.3 Literature models correlation for Al5083 and R_a=3.2µm.

After understanding the trend for R_a=0.4µm, other tests were done for samples with the same material, Al5083, but with different roughness. Then, a similar approach for curve fitting was performed for new samples with a roughness value of 3.2µm. Subsequently, the results are compared with previous tests and finally with the experiments for R_a=0.4µm. This section aims to understand whether it is possible to develop an *h'* estimating relation for every roughness range and how roughness affects the *h'*.

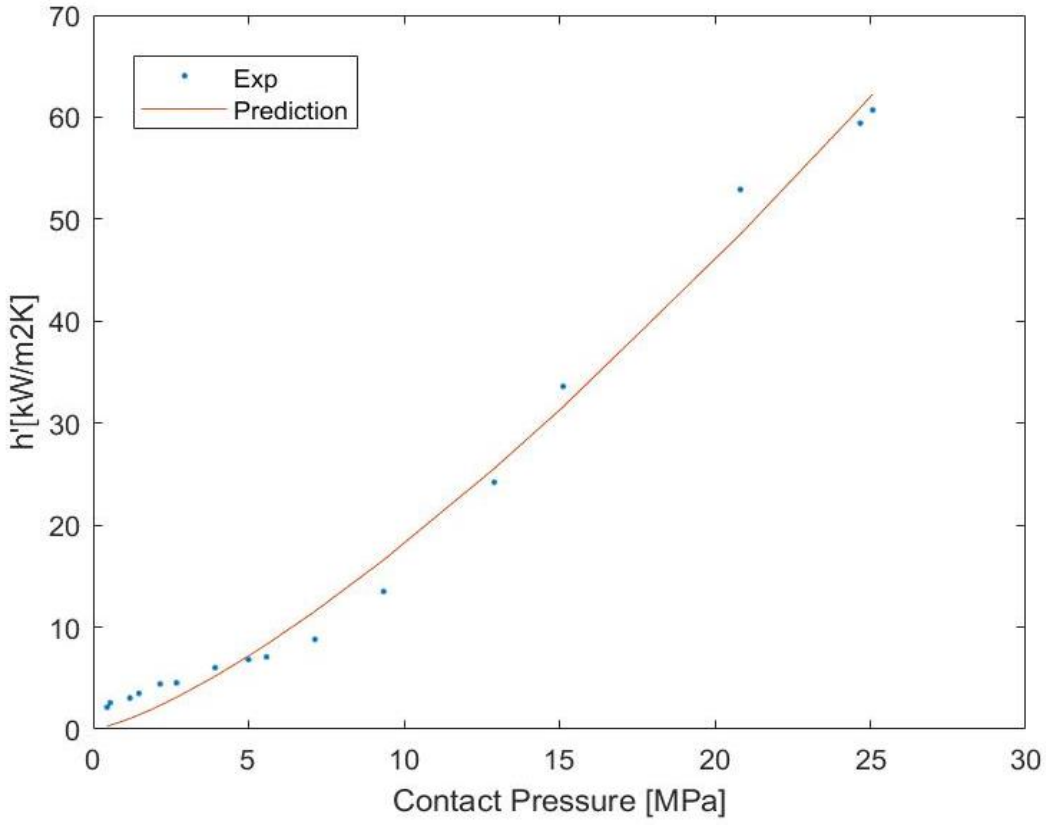

Figure 39 Curve fitting relation for Al5083 3.2µm

Figure 39 plots the fitting curve with equation $h' = Ap^B$ to the experimental values, and the relation which is developed is $h' = 0.811(p^{1.347})$.

The fitting relation here is entirely different from the previous relation. The exponent over pressure(*B*) is also not close to the model values. Also, the '*A'* value is larger than 1, whereas the previous values were less than 1. Therefore, the experimental data points are less to comment on and it needs higher-resolution tests with more data points. Finally, all model predictions are plotted in Figure 41, where it can be observed that in this case the model's predictions are inaccurate.

Another observation is that the trend of *h'* is different up till and beyond 7MPa. Mikic and Yovanovich models do not predict well after 7MPa[3]. Therefore, different fits are done for the readings less than 7MPa and more than 7MPa to compare with the models.

Figure 40 shows the difference in relations and their trend as the slopes are entirely different for both the regions. For more than 7MPa, the relation is found as $h' = 0.71(p^{1.39})$, which is almost similar to the overall prediction fit. For less than 7MPa, $h' = 2.35(p^{0.72})$ the curve is fitting quite well but when the pressure is more then 7MPa there is a mismatch in predicting the range of heat transfer coefficients by models. Data clearly shows that the predicted trend is not valid on these tests

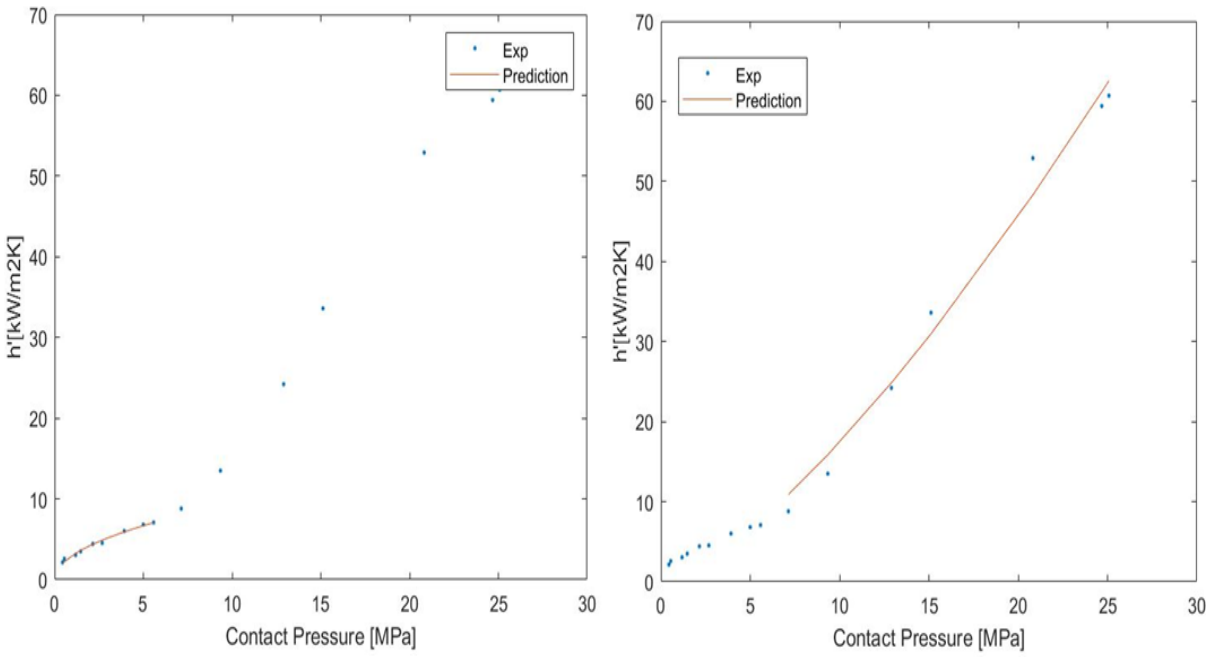

Figure 40 Curve fittings for (i)Till 7MPa (ii)Above 7MPa

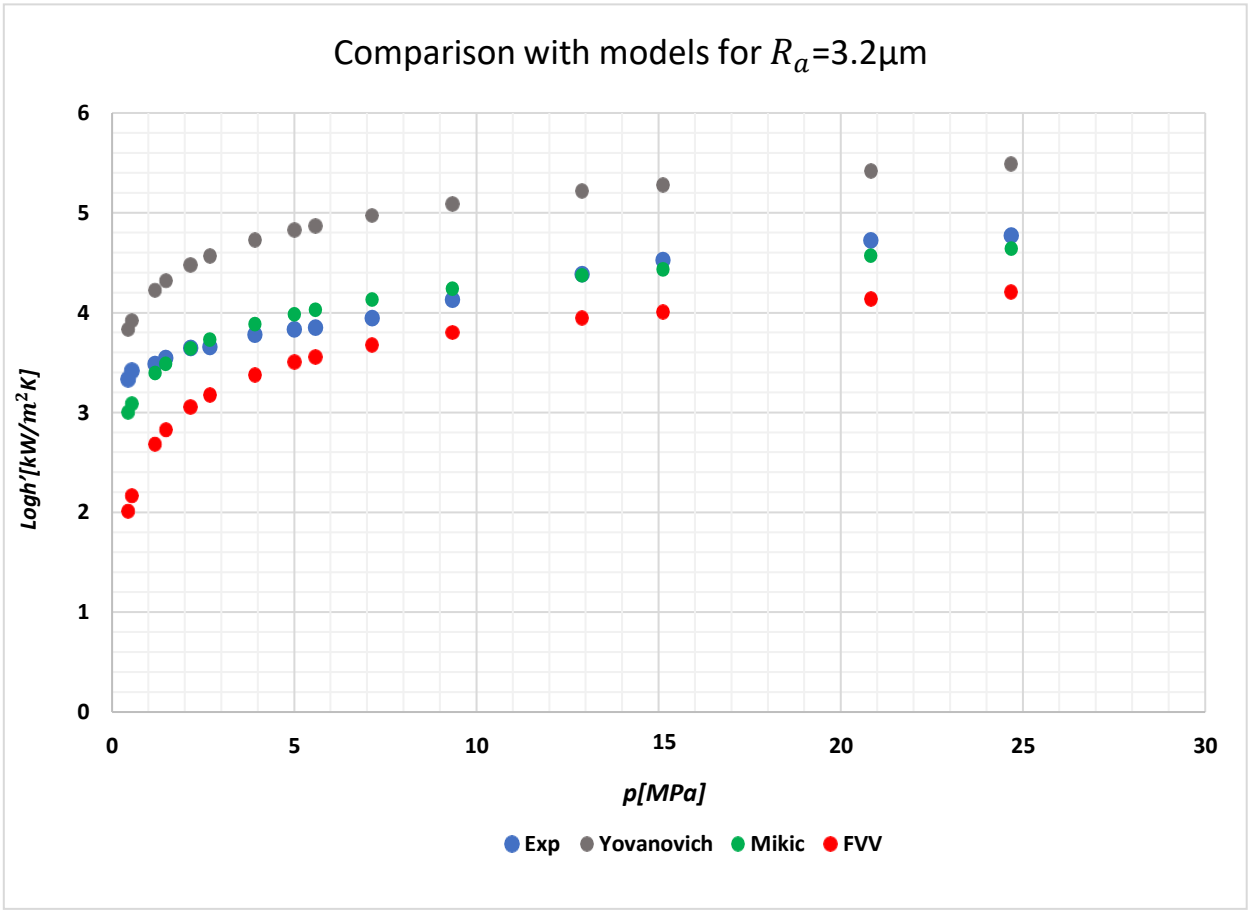

Figure 41 Model comparison Al5083 3.2µm

The closest prediction by the literature model is by Mikic, but the difference changes with contact pressure. So, the trend has changed completely. FVV and Mikic are underpredicting and does not match the expectation after referring to the previous outcomes. The relation prediction is just the curve fitting by the least square fit method. Figure 42 depicts that Mikic predicts well uptill the 7MPa(application range) but later it is entirely different. For R_a=3.2, we cannot develop any relationship and it needs more data points to understand the trend. After correlating the tests, several conclusions can be derived and stated in chapter 5. The conclusion here is that the models cannot be used outside their application range as there is huge mismatch observed and development of empirical relation for this roughness(sample set) is not possible.

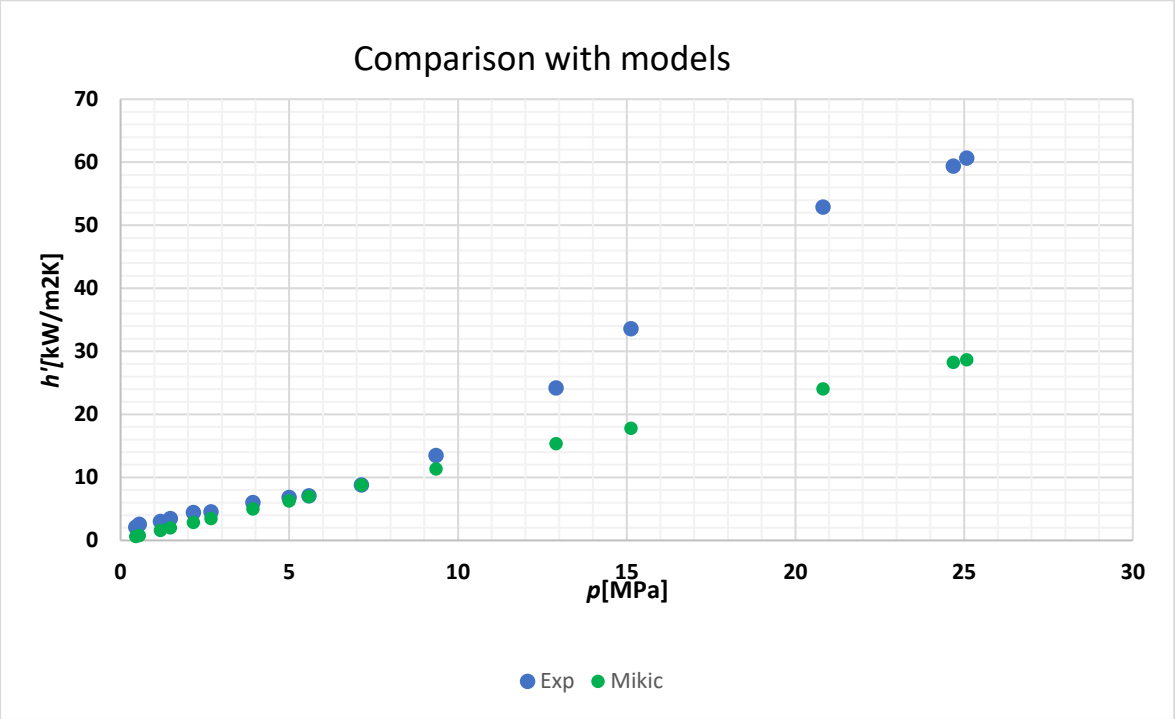

Figure 42 Mikic comparison with experimental value

4.3 Experimental Campaign 2

These experiments aim to understand the effect of aluminum oxide layer formation and orientationeffects.

4.3.1 Experimental Plan

Contacts 1: The samples are cleaned with Isopropanol (IPA). It does not react with the aluminum oxide layer but removes dust and dirt. To measure *h'* for contact pressures,

p=[0.5 1 5.5 12 15 19.5 25] MPa

Contacts 2: Tests will be performed after rotating the bottom sample 90 degrees to check the effect of orientation/alignment. To measuring *h'* for contact pressures,

p=[0.5 1 5.5 12 15 19.5 25] MPa

4.3.2 Outcomes and comparison with literature.

Figure 43(a) includes the plot for contacts 1 in orange, these are the tests performed in the first part of the campaign where we assume that there is no oxide layer formation. The plot with other experiments shows that the results are reproducible, but there can always be a polynomial fit for several points. It can be concluded that within 30 days, there is a significant change in the *h'*. For the contacts 1, initially the value of *h'* is quite low which might be an effect of the oxide layer. But after a certain pressure, around 7 MPa there is change in slope and the conductivity is similar to previous experiments. Thus we can speculate that the oxide layer breaks off when the slope changes respectively.

The TCC is non-reproducible phenomenon but the test setup remains reproducible. The generated empirical relation is plotted along with previous experimental results in the second part of the Figure 43. It can predict the *h'* range in good order and may be used as a reference for future tests. The second part of the experiments is done to understand the change in *h'* due to rotation of alignment/ orientation.

The bottom sample was intentionally rotated to 90 degrees with respect to the top sample to generate different contact. Figure 43(b) plots the results (before and after the rotation) along with the empirical relation prediction and all the experimental results until now. The results of rotation are denoted by Contacts 2 in green.

It can be concluded that the change in orientation of this sample set is not affecting the *h'* and is still in the same range. Also we speculate that the oxide layer has been wore off in contacts 1 and the results for the pressures less then 7MPa are in the same range of the relation unlike contacts 2.
This chapter helped to develope a deep understanding of *h*' for Philips setup.
The series of events helped to learn about model predictions, reproducibility of Philips setup, the assumed effect of the aluminum oxide layer on aluminum samples and orientation/alignment. Therefore, the number of data points are enough to speculate that the *h'* value increases with increasing contact pressure and vice versa.

Moreover, the developed empirical relation is specific to the setup, and predictions are in good order for Al5083 specific samples(45-46) with a R_a value of 0.4µm.
The relation has been developed with more than 60 data points and considers other data from Kawalec. The future tests at Philips are expected to lie within the range estimated by the relation specific to the material, sample number and roughness. In the next chapter, all the results and recommendations for future scope in this field will be discussed in depth.

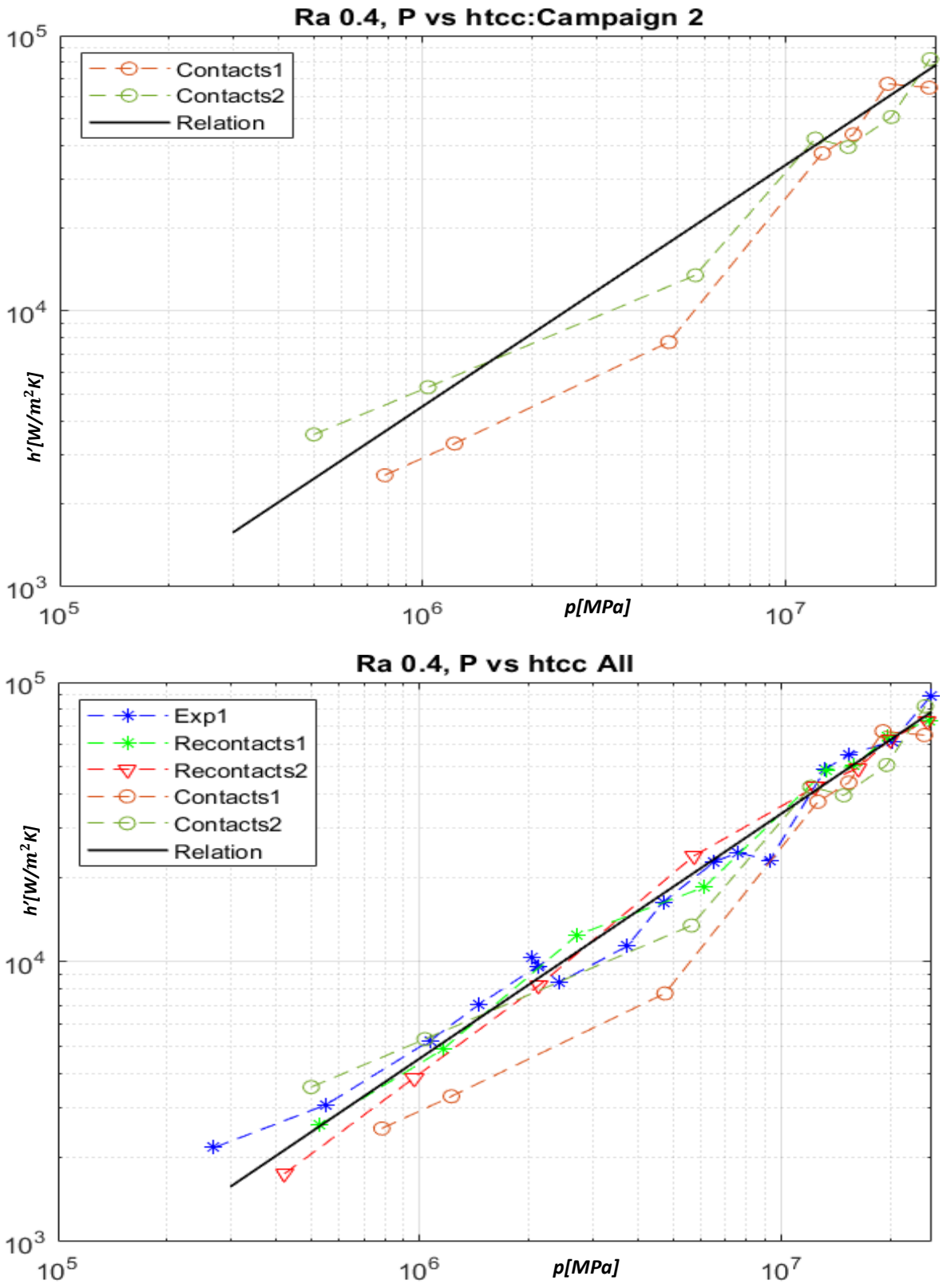

Figure 43 (a) (b) Reproducibility and orientation effects on aluminium after a month

5 Conclusion and recommendations

The thermal contact conduction phenomenon has been in investigation for decades, and the models available in literature are the source to predict contact heat transfer. Research questions discussed at the end of chapter 2 have been answered along with the research.

Identify the need to develop a whole new model for *h'* prediction and its feasibility.

It can be derived from sections 4.2 and 4.3 that the experimental setup is reproducible for aluminium 5083 and roughness factor(R_a) 0.4µm. Previously the reproducibility was not observed for the experiments done in Philips 2019[14]. It was hypothesised that this was due to changing surface conditions of the samples used(i.e. oxidation). As we see from Baharami[10] and section 2.3.1. However, for this sample set it is clear that even after rotating the bottom sample and checking for alignment, the results are still in good order[Figure 43].

It can be speculated that reproducibility was not observed in previous tests as the samples were new, and after some tests, the surface was plastically deformed, and there were no further changes when more tests were performed. Hence, the setup is reproducible.
Several tests are done on the Philips setup to check reproducibility, and also data from another operator is used to verify. The empirical relation developed in section 4.2.1 is in good order with all the experimental values. The developed relation is $h_{contact} = 1640.67\left(\frac{p}{H_c}\right)^{0.8760}$
It is particular to Al5083 material with the roughness value(R_a) 0.4µm. It cannot be used for even different sample set, as seen in section 4.2.2. The development of this empirical relation is very specific, and the development of generic model is complex and require a lot more experimentations.

What Equation or which model can be taken as a reference equation to form the empirical relation?

Section 4.2.1 explains the relationship between surface roughness values with *h'* predictions from different models. We observe that roughness relations are different for all models and no general relation can be derived.

Does change in materials alters the TCC prediction? If so, which material properties effects most?

The factors affecting *h'* can be used to develop a relation taking reference from previous models. The material properties do effect the *h'*, but microhardness and asperity slopes effects more than the bulk hardness. There might be large non-reproducibility that can occur upon recontacts and changing the surface conditions(e.g. new sample). The change in slope observed is due to change in type of deformation from elastic to plastic as discussed in Chapter 3.
Also, chapter 3 and 4 shows that different experimental setups work differently but the procedure to determine *h'* remains unchanged.

To Identify the reason behind the change in slope after certain pressure in prediction of TCC.

The setup in TU Delft[P&E] proved to be a milestone in understanding the deformations and its effects on *h'*. Chapter 3 concludes that when the deformation is in elastic range then increasing load pressure proportionally increases the contact conductance. If the plastic deformation limit is reached at surface locations, after unloading it should not result in decreased contact conductance at previous contact pressures as the effective contact area has increased. Figure 23 and 24 shows that there is a change in slope observed while there is change in deformations from elastic to plastic.

Best method to fit data for correlation (curve fitting, randomization, data analyses or some other methods).

The curve fitting method used here is least square fit.

In section 2.3.1, it is shown that many factors contribute to uncertainty in calculations of *h'*, which varies according to the experimental setup used. Therefore, determining the uncertainty is challenging for different experimental setups. It is difficult to incorporate a generalised error range in calculations. Figure 17 displays the error range of the experiments performed in Philips and is particular to specific material and set-up. Defining general uncertainty range for all set-ups is impossible. Thus, the usage of models for determining contact conductance should be critically analysed.
Developing a generic model for *h*' prediction is extremely challenging due to non-reproducible nature of TCC. The specific database development will be better for company's use case combined with proper thermal design, i.e. the design should not be made such that the TCC is dominant in any heat transfer path.

Future recommendations:

The current study revealed that understanding the real morphology of the surfaces in contact will play a major role in understanding the *h'* effects. The contact pressures above 25MPa should be considered as they are used in ASML and in several energy industries for I.C. engines, turbines, etc.

Future research could further examine the development of semi-empirical relations for specific material-roughness set which is most used in industry. There is a need for more experiments with different roughness and metals that will contribute to a deeper understanding of *h'* and its behaviour with different parameters.

Developing a database set specifically for ASML could also contribute to more accurate predictions for heat model and designing. Finally, for systems where performance by TCC is dominated, it is advised doing sensitivity studies to investigate the impact of TCC behaviour and to design such that performance is not impacted by changes in the TCC between surfaces.

Bibliography

[1] ASML [Online]. Available: https://www.asml.com/en/company/sustainability.

[2] A.F.Mills and V.Ganeshan, Heat Transfer, 2nd edition: Pearson College Div, 1998.

[3] Victor Ustinov, "Experimental Investigation and Modeling of Contact," RWTH Aachen, Aachen , 2018.

[4] ALBIN K. J. HASSELSTRÖM and U. ESKIL NILSSON, "Thermal Contact Conductance in Bolted Joints," Chalmers University of Technology, Gothenburg ,Sweden, 2012.

[5] L. Fletcher and Donald A. Gyorog, "Heat transfer and spacecraft thermal control," *Prediction of Thermal Contact Conductance Between,* vol. 24, no. MIT Press ,Cambridge, pp. 273-288, 1970.

[6] M. Mantelli and M. Yovanovich, "Spacecraft Thermal Control Handbook," in *Ch. Thermal contact resistance* , California, The Aerospace Press, E1 Segundo, 2002, pp. 599-638.

[7] V. Antonetti, T. White and R. Simmons, "An approximate thermal contact conductance," *Journal of Electronic Packaging,* vol. 115, pp. 131-134, 1993.

[8] B. B. MIKIC, "Thermal Contact Conductance; Theoretical Consideration," 1974.

[9] J. R. Culham, P. Teertstra and M. M. Yovanovich, "Calculate Interface Resistance," 2004.

[10] Majid Bahrami, "Modeling of Thermal Joint Resistance for Sphere-Flat Contacts in a Vacuum," 2004.

[11] K. S.S., A. P.M. and R. K., Thermal contact conductance for cylindrical and spherical contacts, Heat and Mass transfer 40, 679-688, 2004.

[12] S. Song. and Michael M. Yovanovich, "Relative Contact Pressure: Dependence on Surface," 1988.

[13] H. J, "Thermal contact resistance , A.E.C report number 2079-2," Massachusetts Institute of Technology , 1964.

[14] Rob Van Gils, "TAR THERMAL CONTACT CONDUCTANCE IN VACUUM," ASML, Eindhoven, 2020.

[15] ADEL ABDEL-HALIM HEGAZY, "Thermal Joint Conductances of Conforming Rough Surfaces: Effects of Surface Micro-Hardness Variation," University of Waterloo, Ontario, 1985.

[16] C. Fieberg and R. Kneer, "Determination of thermal contact resistance from transienttemperature measurement," 2008.

[17] A. Adak, "Semiconductor Lithography - Technology Overview," COPPERPOD INTELLECTUAL PROPERTY, 13 December 2021. [Online]. Available: https://www.copperpodip.com/post/semiconductor-lithography. [Accessed 2 10 2022].

[18] Ruiping. Xu, Haidong Feng, Lanping Zhao and Lie Xu, "Experimental investigation of thermal contact conductance at low temperature based on fractal description," 2006.

[19] A. Upadhyay and R. Singh, "Prediction of Effective Elastic Modulus of Biphasic Composite Materials," *Modern Mechanical Engineering,* vol. 2, no. Heat Transfer Laboratory, Department of Physics, University of Rajasthan, Jaipur, India, p. 8, 2012.

[20] M.R.Sridhar and Michael M.Yovanovich, "Microelectronics heat transfer laboratory," Department ofd Mechanical Engineering , Waterloo, Ontario ,Canada N2L351, 1998.

[21] R. M., B. R. and C. K., "Measurement of Thermal contact conductance," *Journal of Material Processings and Technology,* pp. 204-210, 2003.

[22] H. Fenech and W. M. Rohsenow, "Prediction of Thermal Conductance of Metallic Surfaces in Contact," 1963.

[23] M.G.Cooper, B. B. Mikic and Michael M.Yovanovich, "Thermal contact conductance," *International Journal of Heat and Mass Transfer,* vol. 12, pp. 1517-1520, 1969.

[24] "MODEL DEVELOPMENT FOR THE CONTACT PRESSURE DEPENDENT HEAT TRANSFER," *DIPL.-ENG. VICTOR USTINOV;SEBASTIAN G. SCHULZ;PROF. DR. ING ;PROF. DR. ING.,* pp. 142-147, 2007.

[25] MatWeb, material property data [Online]. Available https://www.matweb.com/index.aspx

[26] AZO, material [Online]. Available https://www.azom.com/article.aspx?ArticleID=9120

Appendix

Appendix A

Cylinder Joint Experiment [4]

The paper [4] uses the cylinder joint experimental setup, which is almost similar to the setup at Philips explained in section 3.3.2

The test specimens consisted of two cylinders with a contacting interface of a few mm in diameter. The small contact area allowed for relatively high and equal interface pressures while using low loads. Away from the interface, both specimens had a conical shape with increasing diameter. This allowed for a lower interface pressure and a larger area for applying heat on the top specimen. The two specimens were mounted in a test column together with a heater, two insulating glass fibre plates, two steel cylinders and a piezoelectric force sensor.Here the numbering is denoted by the following parts, 1-Rig, 2-Spacer, 3-Force sensor, 4- Insulation, 5-Heater, 6-Top cylinder, 7-Bottom cylinder, 8-Aluminum plate, 9-Cooled base. A load was applied in the axial direction of the column using a screw rig. The insulating cylinder on the top of the test column was used to prevent heat conduction away from the interface. [4]

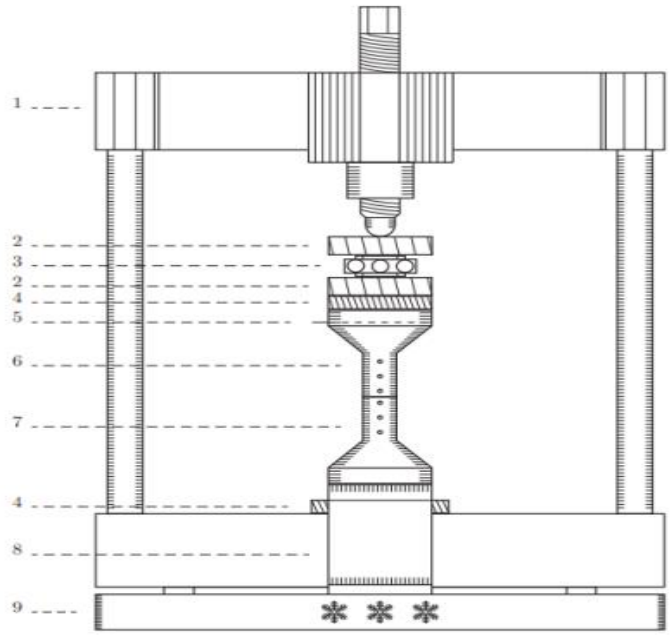

Figure 44 Cylinder Joint experimental setup [4]

The total heat flow over the joint interface can be calculated using the known thermal conductivity of the joint materials and the temperature readings of the top and bottom cylinder thermocouples. The temperature gradients *T/x* are obtained by fitting a least squares line to the three measured temperatures of both cylinders. The average of the two temperature gradients was used because the gradients were thought to be relatively sensitive to possible thermocouple errors. The total heat flow could then be calculated using Fourier's law for one-dimensional flow, which is defined as

$$Q_x = kAt_x.$$

Appendix B

Different types of hardness

Hegazy [15] [16]

There are several ways to measure hardness, the most used are

1. Brinell hardness
2. Rockwell hardness
3. Vickers hardness

Brinell hardness

(H_B)

In this experiment, a ball indenter (usually steel) is pressed against the material with a known load and then the indentation is measured by a microscope. The Brinell hardness can be calculated by the formula

$$H_B = \frac{2L}{\pi D(D - \sqrt{(D^2 - d^2}} = \frac{L}{\pi D t}$$

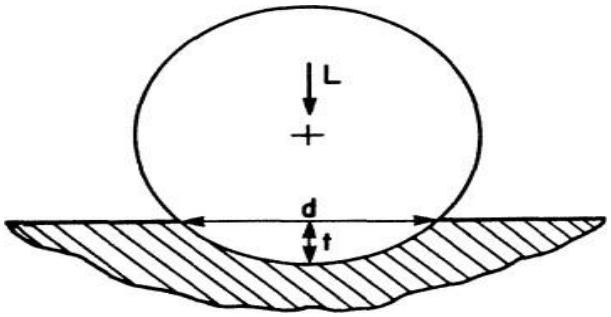

Figure 45 Deformation of flat surface by Brinell ball indenter

Here,

D =Diameter of indenter ball (mm) L=Known applied load (N)

d =Diameter of resulting indentation (mm) t=Depth of indentation (mm)

H_B = Brinell hardness (MPa)

Rockwell hardness

In a similar test as Brinell, the indenter can be changed to a steel ball or 120° diamond cone according to need. However, instead of taking the reference as a flat surface, it takes the reference of indentation with minor load, standard 98.1N, and then a known significant load is applied. Pg. 258 "The Rockwell hardness number is a direct reading from the dial gauge attached to the Rockwell machine while a minor load is still imposed."

According to the Rockwell scale divided into 100 divisions (1 division= 0.002mm), the material is harder if the Rockwell number is higher. Rockwell B and C can be defined as,

$$Rockwell\ B = RB = 130 - \frac{depth\ of\ penetration(mm)}{0.002(mm)}$$

$$Rockwell\ C = RC = 100 - \frac{depth\ of\ penetration(mm)}{0.002(mm)}$$

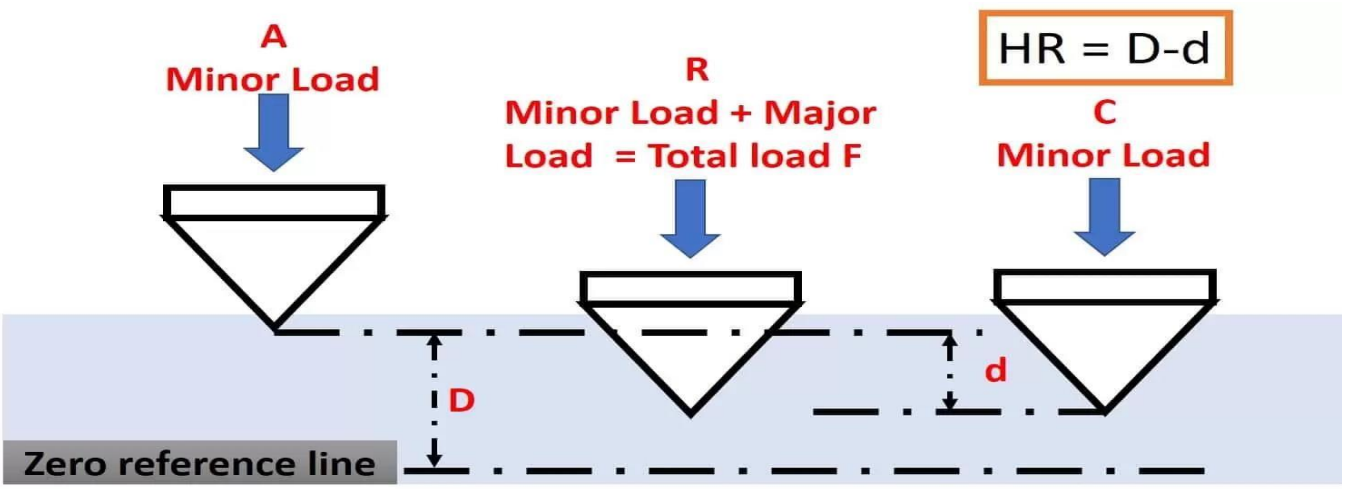

Figure 46 Rockwell hardness test phenomenon

Vickers hardness

(H_v)

A diamond shape polished square base indenter is pressed against the material with a flat surface under a known load. The indentation is calculated by analysing the indentation under a microscope and can be calculated as

$$Hv = \frac{2L\ sin68}{dv^2} = \frac{1.8544L}{dv^2}$$

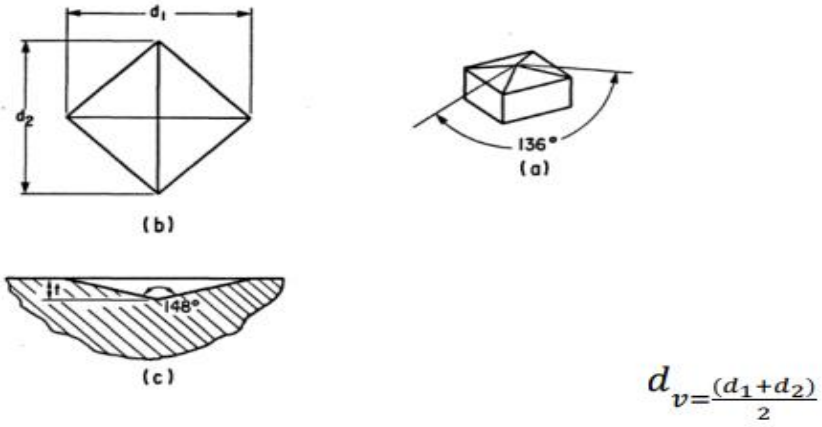

Figure 47 Deformation on flat surface by Vickers diamond

a) Indenter b) Indentation c) Indentation geometry

Here,

L= known applied load (N)

d_v= Mean diagonal of resultant indentation(mm). t= Depth of indentation(mm)

Sin68° = Pg 260 “because the diamond pyramid has an angle of 136° between opposite faces and 148° between the opposite edges.”

Appendix C

Temporal response for round 3 explained:

Isolation cylinder -Tin sample- New 10mm length									Time	60	sec	Tin	16	C	16	C
									Water flow	315	mg or ml	T out	16	C	18	C
									Mass flow rate	0.00525	g/s	Delta T	2	K		
t	T1	T2	T3	T4	T=Tin-(Tin-Ti)*e(-t/Tau)	Residual	Residual^2	Sum(Residual^2)	Power	50%		Q	43.89	Watts		
2	37.2	37	16.7	16.3	42.20703416	-5.00703	25.07039109	202.1882762	Voltage	128	V					
6	77.7	76.8	20.6	19.3	86.83884141	-9.13884	83.51842231		Current	0.76	A				kg	N
10	106.1	104.8	25.5	23.4	109.5040639	-3.40406	11.58765137		Q	97.28	Watt		Weight of cu cylinder		0.34	12.5568
15	131.8	129.6	32.1	29	123.9694694	7.830531	61.31720918		T infinite	144			Weight of heater pla		0.94	
20	134.8	132.5	36.4	32.9	131.3567457	3.443254	11.85600016		Tinitial	4			Weight of nuts *4		0	
25	135	132.7	37.6	34.1	135.4354727	-0.43547	0.189636447		Tau	30			Weight of figure		0	
30	134.9	132.6	38.5	34.9	137.8409124	-2.94091	8.648965628		Area	0.000001	m2	NO LOAD	net Weight		1.28	Kg
									T1-T2	2.3						
									T2-T3	94.1						
									T3-T4	3.6			No deformation			

Isolation cylinder -Tin sample- New 10mm length									Time	60	sec	Tin	16	C	18	C
									Water flow	315	mg or ml	T out	16	C	19	C
25-01-2023									Mass flow rate	0.00525	g/s	Delta T	3	K		
t	T1	T2	T3	T4	T=Tin-(Tin-Ti)*e(-t/Tau)	Residual	Residual^2	Sum(Residual^2)	Power	50%		Q	65.835	Watts		
2	125.1	123.1	37.2	33.6	127.1123528	-2.01235	4.049563678	20.00300082	Voltage	128	V					
6	133.1	132.4	39.3	35.5	134.5929407	-1.49294	2.228872044		Current	0.76	A				kg	N
10	133.8	131.2	40.7	36.7	136.1235679	-2.32357	5.398967951		Q	97.28	Watt		Weight of cu cylinder		0.34	18.29565
15	133.8	131.4	41.1	37.4	136.6854111	-2.88541	8.325597144		T infinite	138			Weight of heater pla		0.94	
									Tinitial	110			Weight of nuts *4		0.2	
									Tau	6			Weight of figure		0.385	
									Area	0.000001	m2		net Weight		1.865	Kg
									T1-T2	2.4						
									T2-T3	90.3						
									T3-T4	3.7			No deformation			

Isolation cylinder -Tin sample- New 10mm length									Time	60	sec	Tin	16	C	18	C
									Water flow	315	mg or ml	T out	16	C	19	C
25-01-2023									Mass flow rate	0.00525	g/s	Delta T	3	K		
t	T1	T2	T3	T4	T=Tin-(Tin-Ti)*e(-t/Tau)	Residual	Residual^2	Sum(Residual^2)	Power	50%		Q	65.835	Watts		
2	131.8	129.5	41.3	37.3	128.0384458	3.761554	14.1492903	14.26428147	Voltage	128	V					
6	132.5	130	42.2	38.5	132.2919306	0.208069	0.043292889		Current	0.76	A				kg	N
10	133.6	131.1	42.7	38.5	133.3322347	0.267765	0.071698281		Q	97.28	Watt		Weight of cu cylinder		0.34	20.74815
									T infinite	135			Weight of heater pla		0.94	P[Mpa]
									Tinitial	120			Weight of nuts *4		0.2	#DIV/0!
									Tau	6			Weight of figure		0.635	
									Area	0.000001	m2		net Weight		2.115	Kg
									T1-T2	2.5						
									T2-T3	87.8						
									T3-T4	3.7			No deformation			

Isolation cylinder -Tin sample- New 10mm length									Time	60	sec	Tin	16	C	18	C
									Water flow	315	mg or ml	T out	16	C	19	C
25-01-2023									Mass flow rate	0.00525	g/s	Delta T	3	K		
t	T1	T2	T3	T4	T=Tin-(Tin-Ti)*e(-t/Tau)	Residual	Residual^2	Sum(Residual^2)	Power	50%		Q	65.835	Watts		
2	123.6	121.7	40.5	36.9	124.9716788	-1.37168	1.881502767	4.877241751	Voltage	128	V					
6	132.4	129.8	42.2	38	132.4110261	-0.01103	0.000121575		Current	0.76	A				kg	N
10	133.1	130.5	43.3	39.5	134.8307852	-1.73079	2.99561741		Q	97.28	Watt		Weight of cu cylinder		0.34	23.20065
					115	-115	13225		T infinite	138			Weight of heater pla		0.94	
									Tinitial	115			Weight of nuts *4		0.2	
									Tau	10			Weight of figure		0.885	
									Area	0.000001	m2		net Weight		2.365	Kg
									T1-T2	2.6						
									T2-T3	87.2						
									T3-T4	3.8			No deformation			

Isolation cylinder -Tin sample- New 10mm length									Time	60	sec	Tin	18	C	18	C
									Water flow	315	mg or ml	T out	18	C	20	C
25-01-2023									Mass flow rate	0.00525	g/s	Delta T	2	K		
t	T1	T2	T3	T4	T=Tin-(Tin-Ti)*e(-t/Tau)	Residual	Residual^2	Sum(Residual^2)	Power	50%		Q	43.89	Watts		
2	39.2	40.3	18.9	18.4	46.68078552	-7.48079	55.96215198	285.7538155	Voltage	128	V					
6	79.1	78.6	24	22.5	91.15309828	-12.0531	145.2771781		Current	0.76	A				kg	N
10	115.5	114.7	31.5	28.8	111.4746985	4.025302	16.20305253		Q	97.28	Watt		Weight of cu cylinder		0.34	25.65315
15	131	129.1	38.3	34.7	123.3581992	7.641801	58.3971194		T infinite	138			Weight of heater pla		0.94	
20	132.1	129.9	41.5	37.7	128.9986415	3.101358	9.61842441		Tinitial	5			Weight of nuts *4		0.2	
25	132.5	130	43.7	39.3	131.9560432	0.543957	0.29588905		Tau	25			Weight of figure		1.135	
30	132.7	130.5	44.4	40.4	133.6379381	-0.93794	0.879727935		Area	0.000001	m2		net Weight		2.615	Kg
									T1-T2	2.5						
									T2-T3	86.3						
									T3-T4	4.4			No deformation			

Isolation cylinder -Tin sample- New 10mm length									Time	60	sec	Tin	16	C	18	C
									Water flow	315	mg or ml	T out	19	C	20	C
25-01-2023									Mass flow rate	0.00525	g/s	Delta T	1	K		
t	T1	T2	T3	T4	T=Tin-(Tin-Ti)*e(-t/Tau)	Residual	Residual^2	Sum(Residual^2)	Power	50%		Q	21.945	Watts		
2	54.8	54.9	22.1	21.5	60.71929499	-5.91929	35.03805321	223.2126125	Voltage	129	V					
6	85.1	83.9	25.6	24.3	97.36427244	-12.2643	150.4123784		Current	0.76	A				kg	N
10	115.5	113.4	32.8	31.3	114.502536	0.997464	0.994934474		Q	98.04	Watt		Weight of cu cylinder		0.34	28.1547
15	130.5	127.4	40.4	36.8	124.7414189	5.758581	33.16125659		T infinite	138			Weight of heater pla		0.94	
20	131.6	128.2	44.4	40.4	129.7010556	1.898944	3.605989861		Tinitial	27			Weight of nuts *4		0.2	
25	131.6	128.2	44.9	41.8	132.3450044	-0.745	0.555031496		Tau	25			Weight of figure		1.39	
30	131.6	128.3	46.6	42.4	133.8691498	-2.26915	5.149040963		Area	0.000001	m2		net Weight		2.87	Kg
									T1-T2	3.4						
									T2-T3	83.3						
									T3-T4	3.1			Deformation 1.94 mm diame			

Experiment vs the models in anti-log scale(Chapter 3)

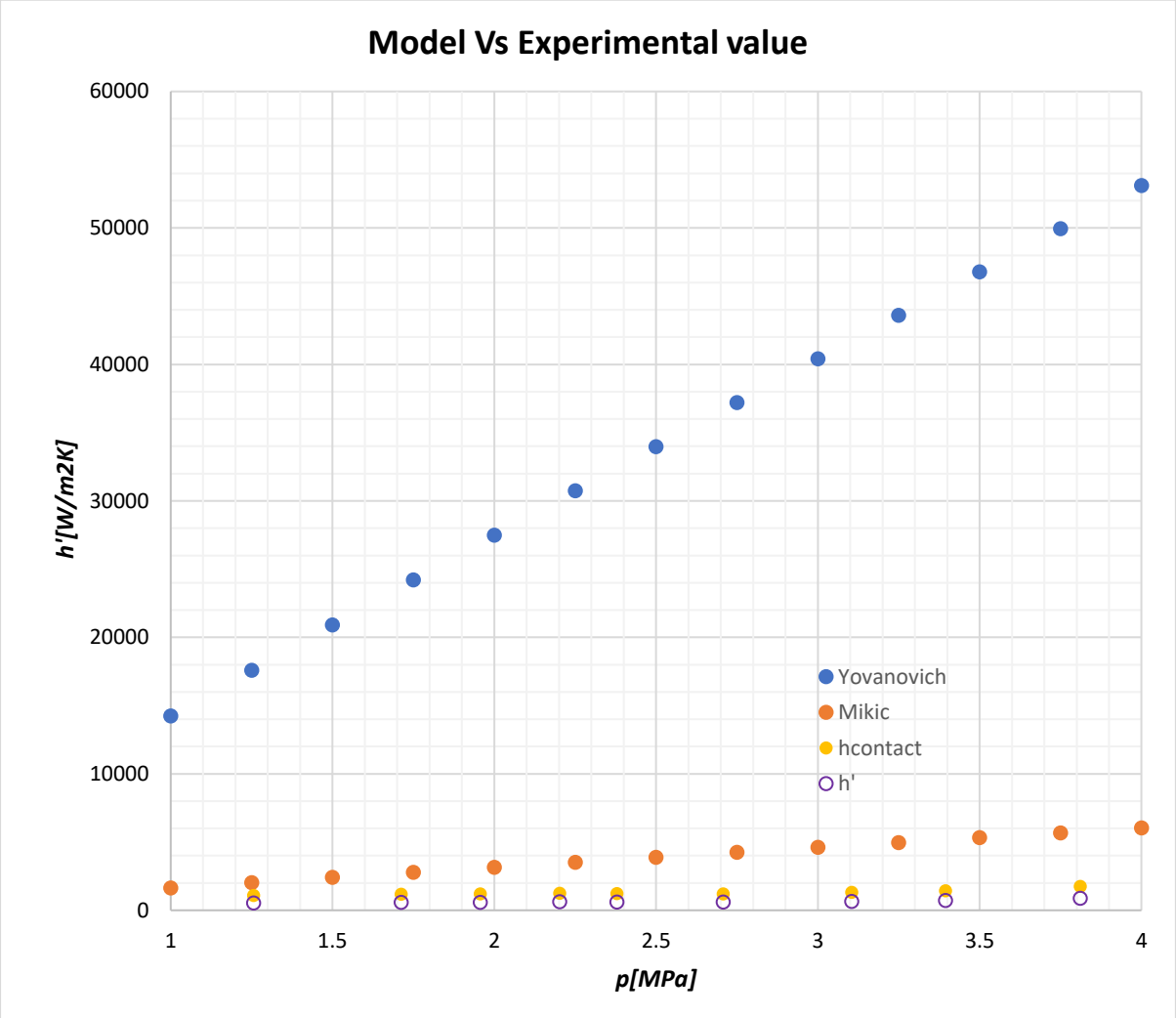

Figure 48 h' vs hcontact with models plot

Appendix D

Lithography [17]

Semiconductor lithography, also known as photolithography, is a fabrication method that goes from highly complex circuit designs drawn on a giant glass plate photomask to a reduced version of ultra-high-performance lenses exposed into a silicon substrate known as a wafer. The light source is projected through mirrors or lenses on the semiconductor chips to draw specific patterns. For ASML, the imprints are on a microscale, and it is essential to understand the behaviour of specific light sources. Figure 49 shows a simple diagram of how light is projected over a wafer using lenses.

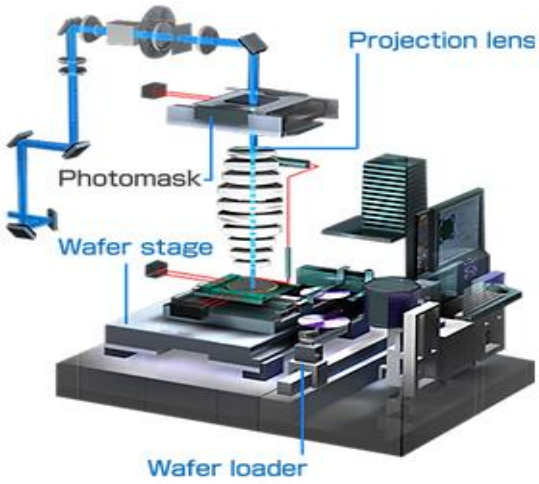

Figure 49 Lithography Setup

EUV, or extreme ultraviolet lithography, is a technique or process that employs extreme ultraviolet lithography light with a very short wavelength of 13.5 nm. With the advancement of EUV lithography, Moore's law is also being applied. This lithography technique is intended to revolutionise the dynamics of cutting-edge semiconductor manufacturing.

The EUV Lithography technique enhances or boosts the upcoming scaling demand for the printing of miniature features. In addition, with the help of this technique, tool manufacturers have significantly reduced the wavelength, which is extreme UV, for the light used to implement imaging systems.